
Copyright Undertaking

PVDF THIN FILM AND NANOFIBERS FOR ENERGY APPLICATIONS

SONG RUOBING

M.Phil

The Hong Kong Polytechnic University

2016

The Hong Kong Polytechnic University

Department of Applied Physics

PVDF Thin Film and Nanofibers for Energy Applications

SONG Ruobing

A thesis submitted in partial fulfillment of the
requirements for the degree of Master of Philosophy

August 2015

CERTIFICATE OF ORIGINALITY

I hereby declare that this thesis is my own work and that, to the best of my knowledge and belief, it reproduces no material previously published or written, nor material that has been accepted for the award of any other degree or diploma, except where due acknowledgement has been made in the text.

(Signed)

SONG Ruobing (Name of student)

Abstract

The increasing demands for clean, reliable and sustainable energy require researchers to develop highly efficient and environmentally friendly energy harvesting/storage devices. Nowadays, renewable energy already occupies a bigger share of the world's energy demand pie, and still keeps growing. Mechanical and solar energy are ubiquitous in our daily life. In this work, we focus on studying the use of Polyvinylidene fluoride (PVDF) as a component in the mechanical and solar energy harvester. PVDF has attracted extensive interest for decades due to its unique piezoelectric and ferroelectric properties, high chemical and thermal stability. In addition, PVDF is intrinsically an organic, which allows it to be fabricated by low-cost methods and engineered to be PVDF thin film or PVDF based nanofiber.

Recent works have shown considerable attention towards self-powered energy source by scavenging energy from ambient environments. The integration of energy harvesting and energy storage device is a way that not only enables to convert ambient energy into electricity but also provides sustainable power source for various electronic devices and systems. It is highly desirable to improve the integration level and minimize unnecessary energy loss in the power-management circuits between energy harvesting and storage devices. In our study, we fabricated a device composed of supercapacitor and piezoelectric nanogenerator. PVDF thin film membrane was integrated as a component both the separator and the energy harvester in a supercapacitor to form a rectification-free devices for one-step energy conversion and storage. In this device, externally mechanical impact establishes a piezoelectric potential across the PVDF film, which serves as a driving force for the migration of ions towards the interface of functionalized carbon cloth electrodes and stores the electricity in the form of electrochemical energy.

Transparent electrode is an indispensable component for solar cell. The thin and flexible transparent electrodes with excellent conductivity and good transmittance are highly desirable in industry. Ag nanofibers (Ag NFs) networks have been shown with high transmittance, low resistance and excellent flexibility. The contact resistance between two nanofibers junction hinders the further reduction of the sheet resistance of Ag NFs networks. In our work, Ag NFs electrode was produced by combining electrospun PVDF nanofibers with electroless metallic deposition technique. The fabrication parameters of PVDF nanofibers were systematically investigated for obtaining high quality nanofibers. Then, the PVDF nanofibers worked as template for the Ag electroless deposition at ambient temperature.

List of Publications

1. **R. B. Song,** , H. Y. Jin, X. Li, L. F. Fei, Y. D. Zhao, H. T. Huang, H. L. W. Chan, Y. Wang, and Y. Chai. “A rectification-free piezo-supercapacitor with a polyvinylidene fluoride separator and functionalized carbon cloth electrodes” *Journal of Materials Chemistry A,* **3**, 14963-14970. (2015).

2. **R. B. Song**, F. Y. Gu, Y. Chai, “Transparent Conducting Nanofiber of Electrospun PVDF/$SnCl_2$ with Ag for electrode application.” (Prepared to submit)

3. L. F. Fei, Y. M. Hu, X. Li, **R. B. Song**, L. Sun, H. T. Huang, H. S. Gu, H. L. W Chan, and Y. Wang. "Electrospun Bismuth Ferrite Nanofibers for Potential Applications in Ferroelectric Photovoltaic Devices." *ACS applied materials & interfaces,* **7**, 3665-3670. (2015).

4. L. T. Shen, Y. D. Zhao, Y. Wang, **R. B. Song**, Q. Yao, S. S. Chenand Y. Chai “A long-term corrosion barrier with an insulating boron nitride monolayer." *Journal of Materials Chemistry A* (2016)

5. X. L. Yu, B. Cai, **R. B. Song**, Z. B. He, S. S. Guo, X. Z. Zhao, H. L. W Chan, and Y. Wang, “Ferroelectric Nanofibers promote Cancer cell migrations: synergistic effects of aligned topography and electrical charges” (Prepared to submit)

Acknowledgements

I would like to express my most sincere appreciation to my supervisor, Dr. Y. Chai, for his invaluable direction and constant support throughout the whole academic research work. I cannot smoothly accomplish my study without his broad academic knowledge and valuable guidance. He has always been kind and patient to me. I really cherish the scientific thinking and method learned from him. The systematic academic training would accompany me in my future career life.

I would also like to thank Dr. Y. Wang, for giving me the opportunity to study in Hong Kong Polytechnic University and for his academic advising and help during my MPhil study.

I would also like to thank my co-supervisor, Dr. H.T. Huang, for his helpful discussion about the rectification-free piezo-supercapacitor.

I would like to give my thanks to my group mates and colleagues Dr. L.F. Fei, Dr. N.Q. Fu, Mr. X. Li, Mr. Z.H. Yong, Mr. H.Y. Jin, Mr. Y.D. Zhao, Mr. M.H. Wong, Ms.Y. Liu, for their useful help and discussion in experiments. Many thanks to my friends for their constant accompany and support in my life in Hong Kong.

Finally, I sincerely thank my parents for their loves, encouragement and for being understanding, patient, supportive during these two years of MPhil studies.

Table of Content

Chapter 2

A rectification-free piezo-supercapacitor with a PVDF separator and functionalized carbon cloth electrodes 62

Chapter 3

Transparent Conducting Nanofiber of Electrospun PVDF/$SnCl_2$ with Ag for Electrode Application 91

Chapter 4

List of Figures

List of Tables

List of Abbreviation

Abrreviation	**Description**
LEDs	Light-Emitting Diodes
LCDs	Liquid Crystal Displays
ITO	Tin-doped Indium Oxide
RF	Radio Frequency
PVDF	Polyvinylidene Fluoride
P(VDF-TrFE)	Poly(vinylidenefluoride-co-trifluoroethylene)
NFES	Near-Field Electrospinning
EDLC	Electric Double Layer Capacitors
PANI	Polyaniline
PPY	Polypyrrole
PEDOT	Polyethylenedioxythiophene
PEDOT:PSS	Poly(3,4ethylenedioxythiphene)poly(styrenesulfonate)
PTH	Polythiophene
ESR	Equivalent Series Resistance
PCC	Pure Carbon Cloth
FCC	Functional Caron Cloth
SCPC	Self-Charging Power Cell
Ag NWs	Ag Nanowires
Ag NFs	Ag Nanofibers
PET	Polyethylene Terephthalate
XRD	X-Ray Diffractometric
SEM	Scanning Electron Microscopy
CV	Cyclic Voltammetry
GCD	Galvanostatic Charge and Discharge

EDS	Energy Dispersive Spectroscopy
UV-vis	UV-2550 Spectrophotometer
TCEs	Transparent Conducting Electrodes
EAD	Electroless Ag Deposition
ECD	Electroless Copper Deposition
Na-RGO	Na-reduced Graphene Oxide

Chapter 1. Introduction

1.1 Foreword

Modern life has become more convenient and colorful with the rapid development of modernization, industrialization, and urbanization. These changes also lead to serious “energy crisis” [1]. There are of great urgent need to discover and apply some environmentally friendly, sustainable, and renewable source of energy (including wind, solar geothermal, nuclear and hydropower, etc.), which has been stimulating researchers’ great interests to explore and investigate novel technologies associated with energy conversion and storage [2–13].

“Energy harvesting” has been proposed for almost two hundred years [14]. Usually, energy harvesting is a process that converts ambient environment energy sources (e.g., mechanical, solar, temperature gradient, etc.) into useable energies, often in the form of electric energy by using different kinds of technologies (piezoelectric, solar photovoltaics, concentrated solar power system, electromagnetic, and thermoelectric). Among these prevalent technologies, piezoelectric generator has been received growing attention in recent years due to the ease of application and the ubiquitous presentence of mechanical movement. Converting mechanical energy to electrical energy has been an ideal choice for many portable applications, especially for wireless sensor networks, and wearable electrical devices [15,16] .

Energy storage system is equally important to energy harvesting technology. Supercapacitors, or electrochemical supercapacitors as another energy storage system, have attracted more attention in recent years, mainly due to their quick charge-discharge capability, high power density, and long life cycle [17–22]. The development of long-lasting, light-weight and high power density supercapacitors is of great technological importance for critical applications. Recently, a novel design has been proposed that directly hybridized the two process of energy harvesting and energy storage into one. Energy is directly converted and simultaneously stored as electrochemical energy. Energy generator and energy storage device are hybridized as a single and completed unit to be a self-charging battery or supercapacitor.

In addition, harvesting energy directly from sunlight by using solar cell technology has been regarded as another one important way to renewable energy. Thin, transparent, and conducting films are a necessary component for solar cell, and also important for some other modern devices, such as flat panel or plasma displays, touch screen, light-emitting diodes (LEDs), Liquid crystal displays (LCDs) [23]. Over the last decades, there has been a persistent increase in demand of transparent conducting layers for these devices. The dominant materials commonly used today are metal oxide, such as tin doped indium oxide (ITO), and carbon nanotubes, reduced graphene oxide, conductive polymers, as well as metal nanowires. All of these alternatives attract extensive attention to match the rapid development of optoelectronic devices.

1.2 Piezoelectric energy harvesting

Energy harvesting relates to the practice of scavenging low frequency and small amount of energy from ambient environmental sources (e.g., wind, water, heat, and vibration) into some electrical energy by smart and functional materials for directly power electronic system, or for charging electrical storage reservoir [24].

Efficiency is the most important parameter in relation to energy harvesting devices. With the rapid development of new materials and techniques of capturing amounts of energy from the environment, and transforming it into electric energy, some of statistic data with respect to different efficiencies of various "free energy" sources to generate electrical energy are shown in table 1.1[14].

Table 1.1 Efficiencies of various "free energy" sources converted into electrical energy (Source from: Texas Instruments)

Original energy	**Energy conversion approach**	**Efficiency**
Mechanical energy	Piezoelectric system	25-50%
Solar energy	Photovoltaic systems	10-24%
Heat/cold energy	Seebeck elements	0.1-3%
RF(radio frequency) energy	Wireless sensor, WiFi	50%

1.2.1 Mechanism of Piezoelectricity

Piezoelectric energy harvesting is an effective way to directly convert vibratory mechanical energy into electrical energy, which mainly depends on the natural properties of piezoelectric materials. This phenomenon was first found in 1880 by Pierre and Jacque Curie on quartz [24]. Piezoelectric effect exists in two opposite domains, direct piezoelectric effect and converse piezoelectric effect [25]. The direct piezoelectric effect means the electric charge accumulated on the surface of certain materials in response to applied mechanical stress. On the contrary, a piezoelectric material is generated a strain when an electrical field is applied. The directions of the electrical field and mechanical behavior are arbitrary. Therefore, the equations for describing the phenomena are usually expressed with tensors. There has a coupled relationship between the stress and the electrical charge. As show in equation 1.1 and 1.2 [25].

(1.2)

where is mechanical strain, is mechanical stress, E is electrical field, D is electric displacement. The other variables s, e, and d represent material properties, where s is compliance, e is permittivity, and d is coupling matrix depending on unique piezoelectric material. They quantify the relationships between electric and mechanical performance. Mechanical strain is affected by mechanical stress and electric field E. Electric displacement of D is influenced by both mechanical stress and electric field. These two equations describe the transducer and sensor respectively, where mechanical strainand electric displacement D output are resulted from different mechanical stress input, which can be used to describe piezoelectric energy harvesting mechanism.

Piezoelectric materials belong to ferroelectrics. The molecular structure exhibits a local charge separation, which is known as electric dipole [25]. The electric dipoles are randomly oriented at first in the piezoelectric materials, while the electric dipoles reoriented when an external electric field is applied. Once the external poling electric field removed, the dipoles still maintain their orientation. The alignment of the dipole moment may not be perfectly straight because each domain originally has its own directions. The process is shown in Fig. 1.1 [26]. After the poling process, the material can exhibit the piezoelectric effect. An electrical voltage appeared on the surface of the material, when it is subjected with a mechanical stress, as shown in Fig. 1.2 [26]. The gained stable piezoelectric property can be cancelled by heating the material to or above its Curie temperature (*Tc*) or applying another external electric field with opposite direction to the poling one[27].

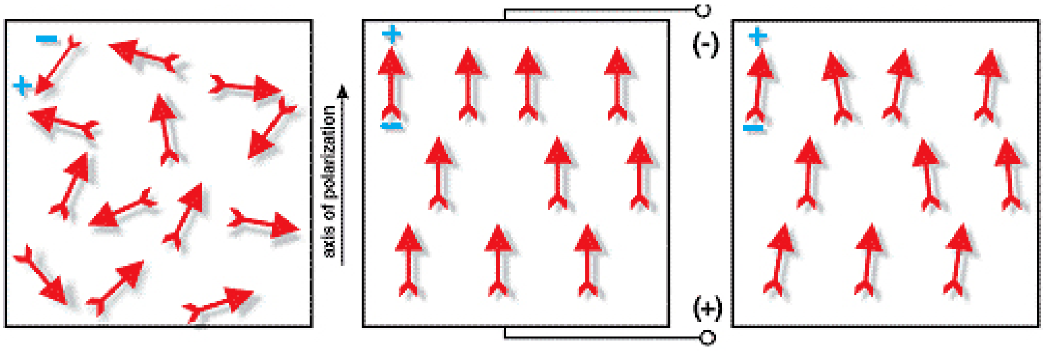

Fig. 1.1 Schematic of poling process (a) original random orientation of polar domains, (b) application of high DC electric field, (c) remnant polarization after the electric field is extinguished[26]

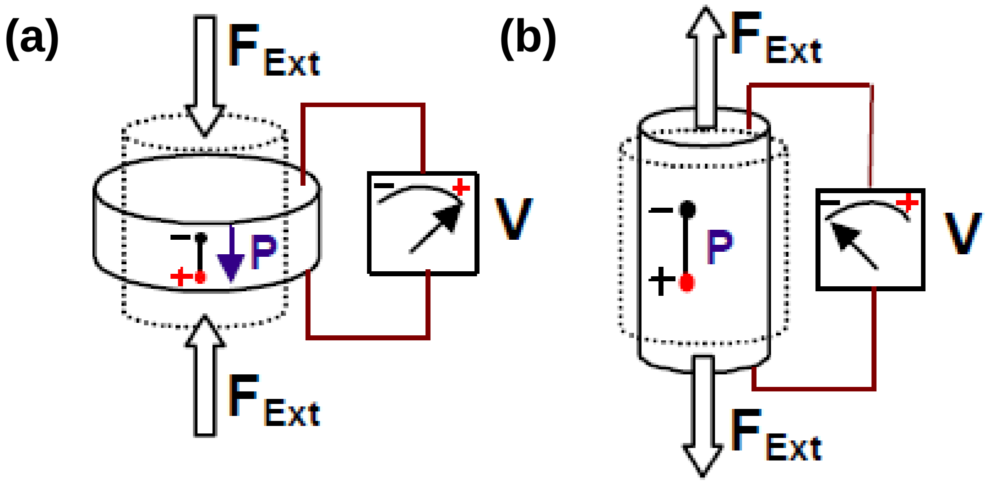

Fig. 1.2 Schematic of direct piezoelectric effect with piezoelectric material in open circuit (a) electric energy generation under compression, (b) electric energy generation under tension [26]

1.2.2 Examples of Piezoelectric materials and its applications

A large number of natural and synthetic piezoelectric materials are available at present[28–35,36]. A brief classification based on inorganic and organic piezoelectric materials is shown in the Table 1.2,

Table 1.2 Classification of piezoelectric inorganic and organic materials

Inorganic	**Organic**
• **Single crystal**: Quartz(SiO_2), sphalerite, Boracite, Tourmaline, Topaz, Sugar, Rochelle Salt, Pyrite, $BaTiO_3$, • **Ceramics:** $BaTiO_3$ ceramic, PZT, PLZT, ZnO, SBT, PBT, NBT, $NaNbO_3$, $ZnSnO_3$	• **Polymers:** PVDF, P(VDF-TrFE), polyparaxylene, poly-bischloromethyuloxetane, aromatie-polyamides, polysulfone, polyvinylfluoride, syntheticpolypeptide

Inorganic piezoelectric materials usually fall into two categories: single crystal and ceramic materials. The first and widely used piezoelectric material is single crystal materials, such as quartz[24]. Although this kind of materials offers a longer life span in terms of sensitivity, their major disadvantage is the low coupling factor, which impede the development in applications. As for ceramics, such as $BaTiO_3$, PZT, $NaNbO_3$, $ZnSnO_3$, and ZnO, which have a higher piezoelectric constant and low manufacturing cost. However, the disadvantage of piezoelectric ceramics is the ease of damage, inflexible, and reliability[25].

Organic piezoelectric materials, such as PVDF, PVDF-TrFE, with the properties of low cost, light weight, high mechanical and chemical stability, excellent flexibility, and ease of fabrication, have attracted extensive attention for these decades[28,29,31,33–35,37–41]. Although the piezoelectric charge constant is lower than that of ceramics, they have much higher piezoelectric voltage constant. Based on these advantages, organic piezoelectric materials have chances to apply in variety flexible and wearable electric applications, such as wearable sensors, ultrasound transducers, flexible actuators, soft-touch switches.

PVDF is one kind of semi-crystalline polymers[42]. There are two regions in the polymers: crystalline and amorphous. Crystallites are dispersed in the amorphous bulk region. The α-phase PVDF is the most stable phase at room temperature[43,44]. Fig. 1.3 shows the polarization schematic of PVDF. When the molecule structure of the PVDF shows the α-phase, the molecular dipoles of this phase are anti-parallel. The chain of the polymer is in the form of TGTG, as shown in Fig. 1.3 (a). After the poling process under an external high electric-field, the crystal structure of the PVDF can be changed from α phase to β phase. The direction of the molecular dipoles of the β phase is parallel and aligned along the vertical direction, as shown in Fig. 1.3 (b). The chain of the β phase is zig-zag configuration TTTT. Therefore, the β phase of PVDF exhibits remarkably piezoelectric properties.

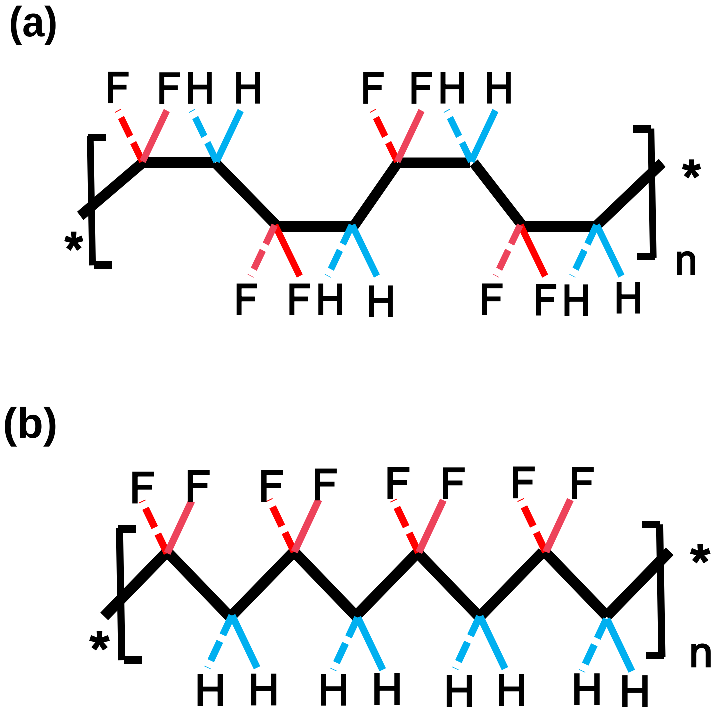

Fig. 1.3 Structures of (a) non-piezoelectric α-phase and (b) piezoelectric β-phase PVDF.

Table 1.3 shows the typical comparison value for some common piezoelectric materials [45]. As we can see, the piezoelectric constant of ceramic PZT is larger than that of PVDF polymer. When the same amount of voltage applied to PZT and PVDF, the generated stain on PZT will be larger than that on PVDF. In addition, the electromechanical coupling constants of PZT is 2.5 times larger than that of PVDF, which means 2.5 times more electrical energy can be transduced from the same mechanical stress for PZT than that of PVDF. However, although PVDF possess a lower piezoelectric charge coefficient and electromechanical coupling constant, its piezoelectric voltage coefficient is around 20 times higher than that of PZT and almost 40 times higher than that of $BaTiO_3$. That means PVDF can be regarded as a better candidate for sensor applications. Furthermore, some properties of PVDF, such as flexible, light weight, and tough, which can fulfill the increasing demands for modern flexible devices.

Table 1.3 Comparison of piezoelectric materials [45]

Property	**Units**	**$BaTiO_3$**	**PZT**	**PVDF**
Density	10^3kg/m^3	5.7	7.5	1.78
Relative permittivity	$\varepsilon/\varepsilon_0$	1,700	1,200	12
Piezoelectric strain coefficient (d_{31})	10^{-12}C/N	78	110	23
Piezoelectric voltage coefficient (g_{31})	10^{-3}Vm/N	5	10	216
Pyroelectric voltage coefficient (P_v)	V/µm K	0.05	0.03	0.47
Electromechanical coupling constant (k_{31})	% at 1 kHz	21	30	12
Acoustic Impedance	(10^6)kg/m^2-sec	30	30	2.7

Choi *et al.* first demonstrated ZnO nanorods based transparent flexible piezoelectric nanogenerator [46]. Fig. 1.4 shows a schematic diagram of integrated transparent flexible current generator with piezoelectric ZnO nanorods and the SEM image of ZnO-nanorod arrays grown on a flexible substrate. This device can generate current through the deformation of piezoelectric ZnO nanorods by external mechanical force.

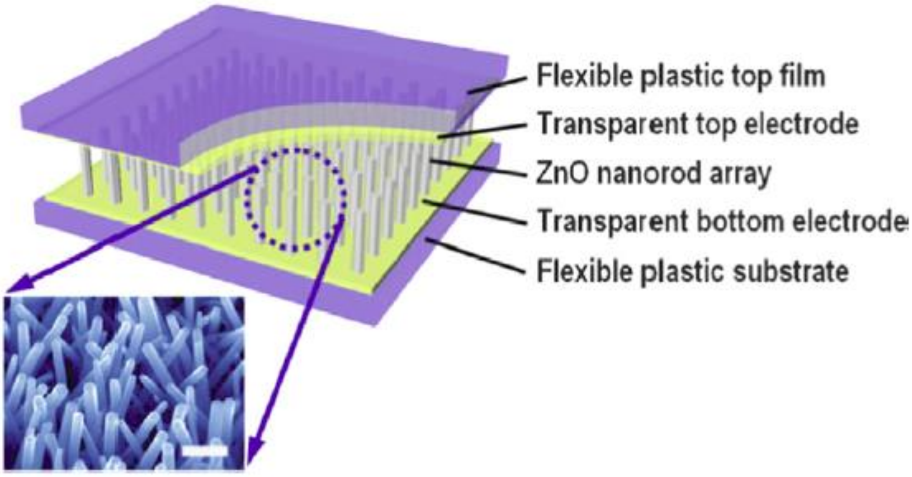

Fig. 1.4 Schematic of the first flexible energy harvester using ZnO nanotods (SEM shown in inset) grown on conductive plastic substrates [46].

Hu *et al.* designed a self-powered system, which can harvest energy from its working environment and store it [47]. The system consists of a piezoelectric nano-generator as a mechanical energy harvester, a capacitor for storing energy, an infrared photo detector as sensor, and a wireless data transmitter for the signal transmission. The integrated system is sketched in Fig. 1.5

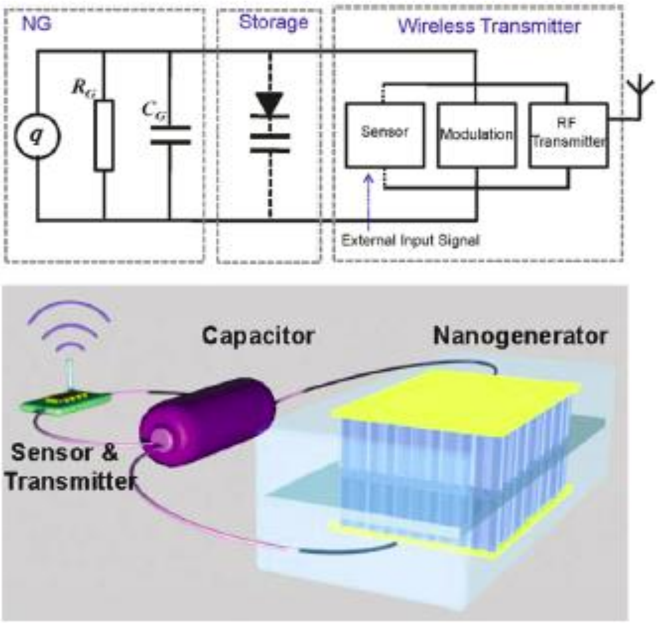

Fig. 1.5 Circuit diagram and schematic of nanognerator used to power a sensor and wireless transmitter therefore acting as wireless sensor node [47].

Chieh Chang *et al.* demonstrated a high energy conversion efficiency PVDF nanogenerator by utilizing near-field electrospinning (NFES) to produce piezoelectric PVDF nanofibers on flexible plastic substrates as shown in Fig. 1.6 [38]. This nanogenerator can be integrated in wireless sensor or self-powered devices. This study also verified that the output voltage and current are respected to the strain rate.

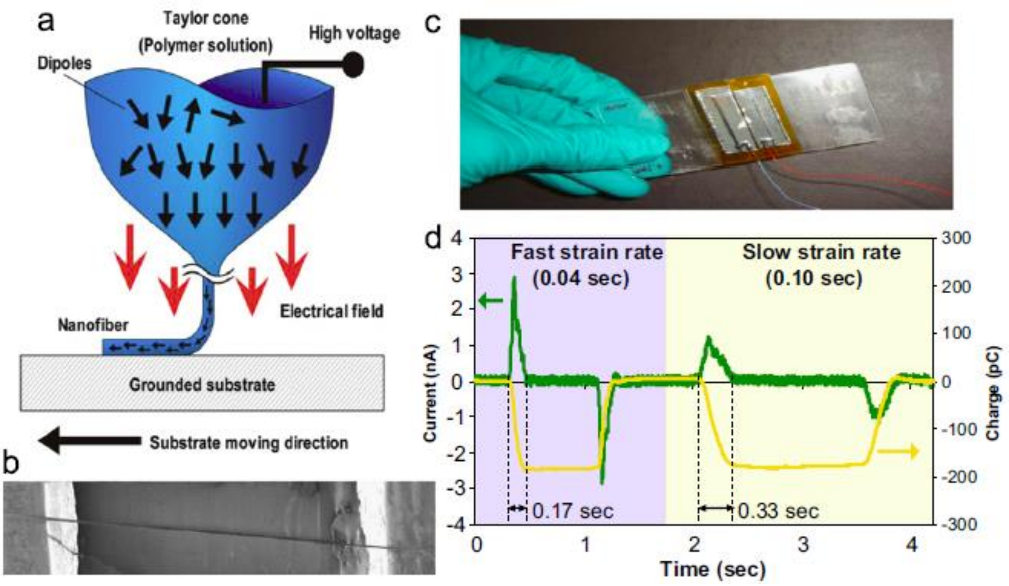

Fig. 1.6 (a) Schematic diagram of the near-field electrospinning process (b) SEM image of single PVDF nanofiber on two contact pades. (c) An optical image of PVDF nanogenerator on the top of plastic substrate. (d) Testing result of the PVDF nanofiber generator under constant mechanical strainrate. As the strainrate increases, higher output current produced while the total charges generate in both cases [38].

。

1.3 Energy storage device—Supercapacitor

1.3.1 Historical Background

Electrical energy storage is required in various applications – activators power source, portable electronic devices (cell phones, laptop, and pagers), standby power for memory devices, and electric hybrid vehicles[48]. The specialized characterization in terms of judgment criteria for the various energy storage devices are energy density (W/g, or W/cm^3), power density (Wh/g, or Wh/cm^3), cost, life span, as well as total weight and whole size. A storage device should meet all the requirements for a particular application.

Traditional capacitors and batteries store electricity in absolutely different ways[49–51]. Batteries have two electrodes, one separator and an electrolyte[49]. Batteries can convert electrical energy into chemical energy with chemical reaction happening involving both the electrodes and the electrolyte, and release it in the form of electrical energy again. Once the chemicals are depleted, the reactions stop and the battery is invalid. The mechanism is shown in Fig. 1.7. Batteries have shown the highest energy density device compared with other energy storage devices [49]. Therefore, batteries are capable to power hybrid vehicles and electronic devices. While the disadvantage of batteries is the low power density, which means batteries cannot produce enough force to drive cars or other automobiles during rapid acceleration[52].

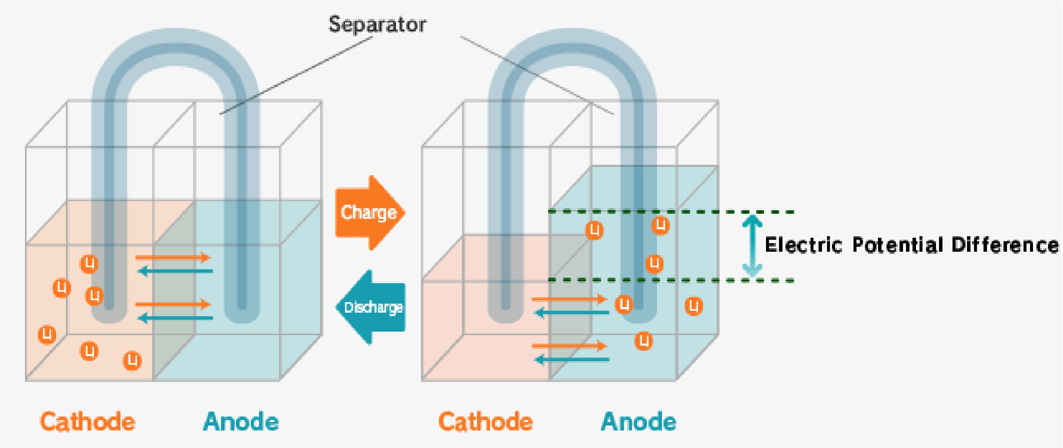

Fig. 1.7 Schematic illustration of a Lithium-ion battery (Picture source from: http://www.eco-aesc-lb.com/en/about_liion/)

However, traditional capacitor possesses high power density, because traditional capacitor adopts static electricity to store energy rather than electrochemical energy [51]. The energy storage mechanism is simply in the form of the positive charges and negative charges on the two metal plates. Therefore, the energy release process is fairly rapid, resulting in the higher power densities and longer life cycles compared with batteries. The structure of a capacitor consists of two conducting metal plates with a relatively thick dielectric insulating separator between them (*e.g.,* ceramic, plastic film, even air). During the charging process, positive and negative charges build up on the two metal plates, respectively, creating an electric field between them. This field polarizes the dielectrics, and the dipoles line up in the opposite direction to the field. Due to the contribution of the polarized dielectric, the plates can store more charge at a given voltage, as illustrated in Fig. 1.8. Therefore, capacitors possess the advantages of light-weight, nontoxic, longer life span, and high power density. However, one big drawback of the capacitor is the inherently low energy density because the energy is stored only between two electrodes, which contribute a small amount of stored energy per unit volume of material and lack of the energy capacity to deliver sustain high-power to all electrical devices[51].

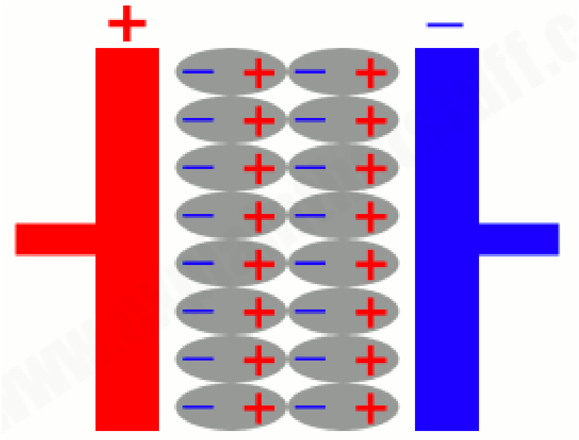

Fig. 1.8 Schematic illustration of a traditional capacitor with dielectric separator (Picture source from: http://www.explainthatstuff.com/how-supercapacitors-work.html)

Supercapacitor, also known as electrochemical capacitor, or ultra-capacitor, offers a solution to the dilemma mentioned above. The power density of supercapcitor is thousands of times higher compared with batteries, and the energy density of supercapacitor is much larger than that of traditional capacitors, which make it become a promising approach to meet the increasing demands of energy storage systems [51]. The earliest patent with respect to supercapacitor was reported in 1957 by H.I. Becker (U.S. Patent 2,800,616) based on high specific area carbon as electrode material [50]. However, Becker's device was not commercialized due to the impractical manufacturing processes. Subsequently, Robert A. Rightmire, a chemist filed another supercapacitor electric device patent in 1962 (U.S. 3,288,641) [50]. After that, SOHIO developed the original carbon double layer capacitors and field as patent (U.S. 3,536,963) [50]. This time, the supercapacitor was endowed with larger value of capacity and the structure format form the basis for the following many hundreds of subsequent design of patents and journal articles. Many different product models were designed and produced from 1980's to meet new requirements of application. An essential fundamental difference of this system was associated with a sequence of redox processes at the interface between electrolyte and electrodes. This redox system gives rise to the larger range of potentials. These developments trigged U.S Department of Energy to propose short-term and long-term supercapacitor programs [53]. In addition, a growing number of patents and journal articles become covered all aspects of supercapacitor technology [21,22,54–60]. Fig. 1.9 shows the comparison of energy density and power density with respect to various type of energy storage devices [5].

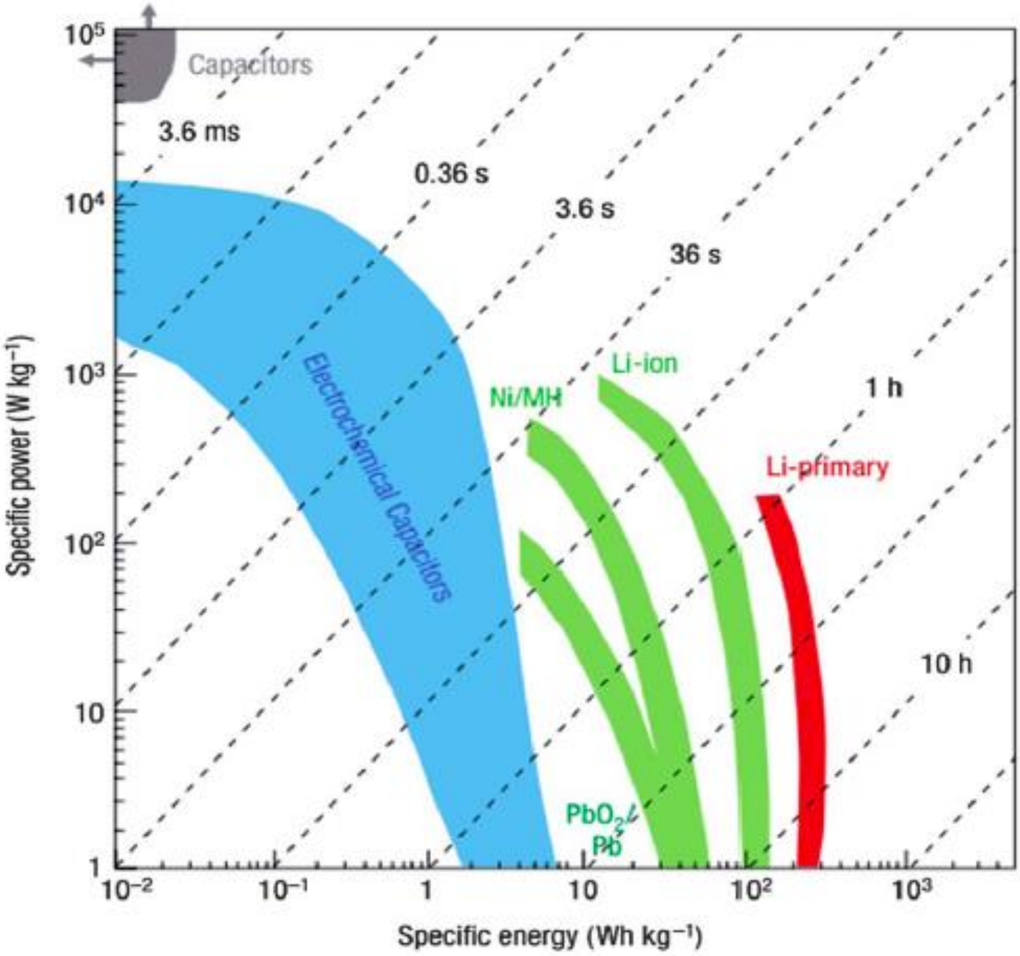

Fig. 1.9 Ragone plot of various type of energy storage devices[5].

1.3.2 Principles of supercapacitor

A typical supercapacitor as a charge-storage device is similar to batteries and traditional capacitor in design, which consists of two electrodes (cathode and anode), an electrolyte, and a porous membrane separator (electrically isolate material allows the migration of ions in electrolyte). According to the different mechanism of storage processes, supercapacitor can be classified into two types: they are electric double layer capacitors (EDLC) and pseudo-capacitors.

1.3.2.1 The mechanism of electric double layer capacitor (EDLC)

Electric double layer capacitor (EDLC) stored energy by electrostatic force (electric ions are of opposite charge adsorbed on the surface of two electrodes.), in which the electrodes are based on electrochemically inactive materials, such as carbon particles[22,61,62]. The structure as shown in Fig. 1.10 [62]. During charging and discharging processes, there is no electrochemical reaction appearance at the interface between electrodes and electrolyte. The increasing of potential drop of the two electrodes purely depends on the physical charge accumulation at the interface. The concept of the electric double layer was first proposed and modeled by Helmholtz in 1853, who stated that the two layers of opposite charge were formed at the interface of electrode/electrolyte, and all the unpaired ions were separated by a specific atomic distance d from the surface of electrode [50,51,53]. This model is similar to that of traditional two-plate capacitors. Three important factors influence the behavior of

EDLC at electrode surface: (1) Electrical potential across the two opposite electrodes; (2) Types of the electrolyte. (3) Surface properties of the electrodes. The capacitance of EDLC can be calculated by the following Helmholtz equation[51]:

$$C=\varepsilon_r\varepsilon_0 A/d \tag{1.3}$$

Where ε_r and ε_o are the electrolyte and vacuum dielectric constants, respectively, d is the effective thickness of the electrical double layer, and A is the surface area of the interface. According to the equation, the specific capacitance C of the supercapacitor is proportional with the specific surface area A and inversely proportional to the atomic distance d. Compare to the traditional capacitor, the electric double layer capacitor yield extremely high capacitance value due to the high electrode surface area A and super diminutive distance d. In the development of EDLCs, carbon-based materials are most widely used as electrodes because of its high surface area and stable chemical or physical activation, and excellent conductivity [19,22,52,59,61–68].

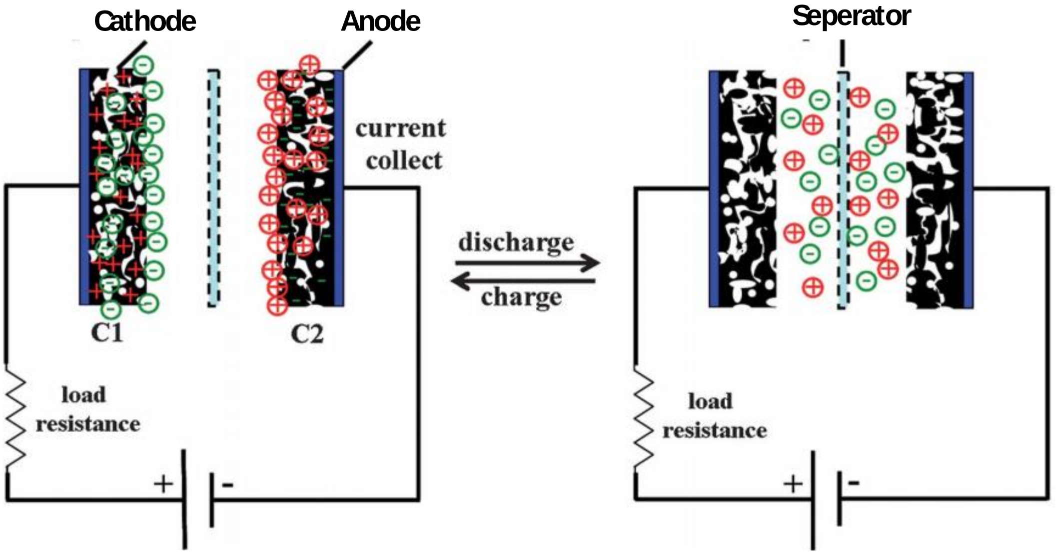

Fig. 1.10 Principles of a double-layer capacitor [62].

1.3.2.2 The mechanism of Pseudo-capacitor

The main difference between pseudo-capacitance and electric double layer supercapacitor lies in the fact that pseudo-capacitance is Faradic [51]. There have fast and reversible redox reactions between the electrolyte and electro-active species on the electrode surface. The mechanism of pseudo-capacitance is similar to that of batteries in charging and discharging process. But the significant difference between pseudo-capacitance and battery is reversibility under charging and discharging processes. The electrodes of battery usually undergo chemical phase changes, which lead to thermodynamic and kinetic irreversibility. On the contrary, there is no chemical phase and composition changes involved in the charging and discharging process of supercapacitor, the whole process is reversible. The cyclic voltammogram curve is a useful criterion and a fundamental characterization to distinguish supercapacitors with batteries. An example of CV curves is shown in Fig. 1.11. The CV curve of RuO_2 pseudocapacitance showed in Fig. 1.11(a) is almost a mirror-type image under charging and discharging process. The CV curve for the battery system of Pb-$PbCl_2$ showed in Fig. 1.11 (b), the potential range for the formation of $PbCl_2$ from Pb is greatly different for the reverse process. The sign of current does not immediately reverse as the direction of sweep voltammetric switching, this phenomenon is in contrary to the behavior observed by RuO_2 (pseudo-capacitor).

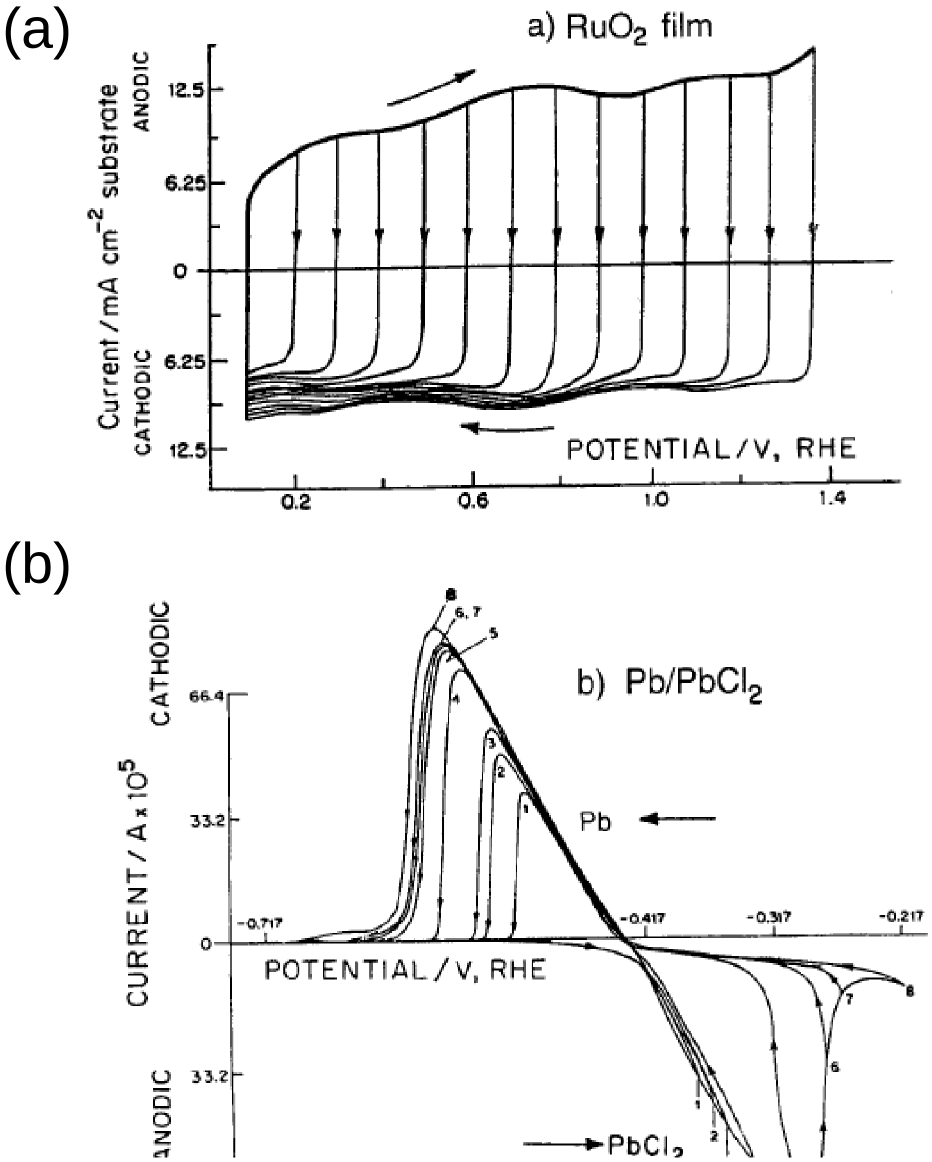

Fig. 1.11 (a) and (b) Cyclic voltammogram curves for RuO_2 and Pb-$PbCl_2$ battery electrode, respectively.

The capacitance of pseudo-capacitance can be calculated by this equation 1.4 [51].

Where represent charge acceptance in the electrodes, and is a charge in potential. The capacitance of pseudo-capacitance can remarkably be enhanced because of the chemical reaction between the chemical-active species on the electrodes surface and the ions in the electrolyte. Conway identified pseudo-capacitance based on three faradic mechanisms: (1) under-potential deposition. (2) redox pseudocapacitance. (3) intercalation pseudocapacitance. These processes are illustrated in Fig. 1.12 [69]. These three mechanisms occur due to different types of materials and different physical processes. Underpotential deposition means different metals form a well absorbed monolayer on their surface above their redox potential. Redox pseudocapacitance occurs when ions in electrolyte adsorbs onto the surface or near the surface of electrodes by electrochemical faradic force. Intercalation pseudocapacitance appeared when ions in the electrolyte can intercalate into the tunnels or layer of electrode materials with no crystallographic phase change.

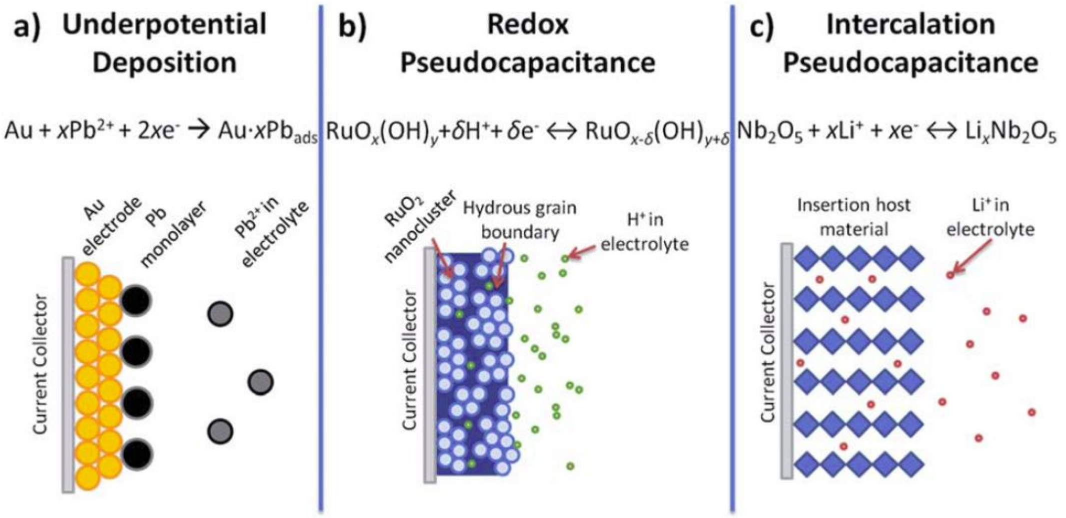

Fig. 1.12 Different types of reversible redox mechanism that give rise to pseudocapacitance (a) underpotential deposition, (b) redox pseudocapacitance, and intercalation pseudocapacitance[69].

Several commonly known active materials that have been widely investigated as pseudo-capacitance electrodes: (1) transition metal oxides (e.g. MnO_2, RuO_2, Fe_2O_3, NiO, Co_2O_3 and V_2O_5 [17,70–75] ; (2) transition metal nitride (e.g. VN, TiN and Mo_2N) [76–79]; (3) conductive polymers (e.g. polyaniline (PANI), polypyrrole (PPY) and polyethylenedioxythiophene (PEDOT) [18,66,80–85].

1.3.3 Key performance parameters for supercapacitor

The basic operation of a single supercapacitor is illustrated in Fig. 1.13 [22]. A simple equivalent circuit consisted of capacitance of anode (C_a), capacitance of cathode (C_c), and equivalent series resistance Rs of the integrated supercapacitor. The capacitance C of the supercapacitor is therefore calculated by the equation 1.5.

The maximum energy density (E) and power density (P) for such a single supercapacitor are given according to the equation 1.6 and 1.7

Where V is the voltage of supercapacitor, C is the total capacitance, and R_s is the equivalent series resistance (ESR). According to these equations, for a supercapacitor possess a good performance, it is important to satisfy the requirements of having a large capacitance value, high operating cell voltage and minimum ESR. Therefore, both electrode materials and electrolyte solutions are required to be investigated in order to optimize the overall performance of the supercapacitor.

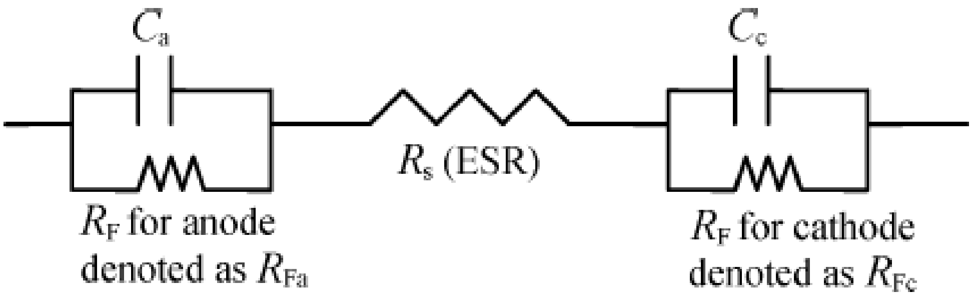

Fig. 1.13 A equivalent circuit representation simple illustrates the basic operation of a single-cell supercapacitor[22]

1.3.4 Classification of supercapacitor based on electrode materials.

In general, electrode materials can be categorized into three types: (1) carbon materials, (2) conducting polymers, and (3) metal oxides, such as RuO_2, IrO_2, MnO_2, NiO, Co_2O_3, SnO_2, V_2O_5, and MoO as shown in Fig. 1.14[19,20,61,86].

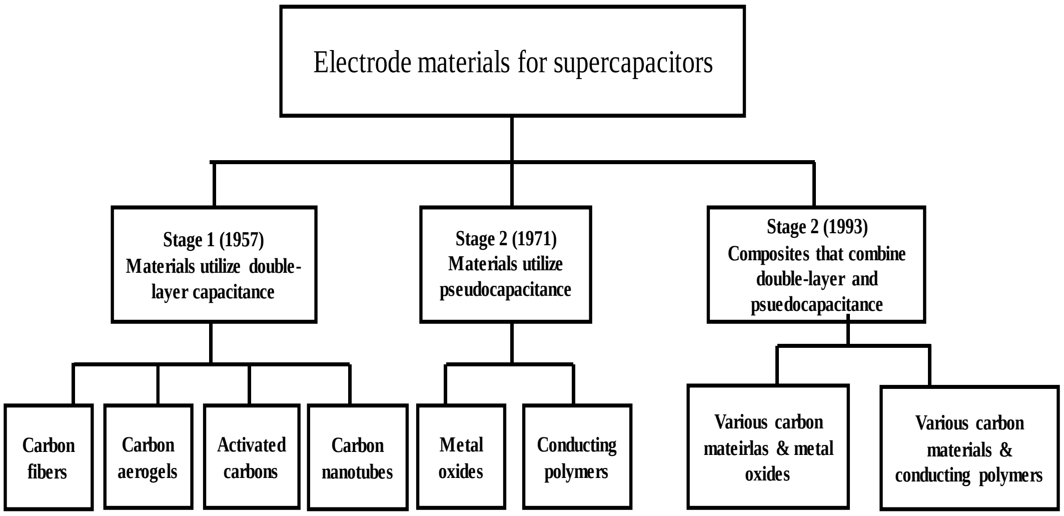

Fig. 1.14 Different materials for supercapacitor [19,20,61,86].

Carbon materials

Carbon materials are prospective electrode materials due to its advantages, such as low cost, abundant, easy fabrication, non-toxicity, higher specific surface area, excellent chemical stability, good electric conductivity[61,87]. Normally, the mechanism of carbon based supercapacitor belongs to EDLS, because it usually form an electrochemical double-layer at the interface between the electrode and the electrolyte. Therefore, the capacitance of carbon-based supercapacitor mainly depends on the surface area accessible to the electrolyte ions. Thus, some important properties of electrodes significant influence the capacitance of supercapacitor. (1) specific surface area, (2) pore-size, (3) pore distribution, (4) pore structure, and (5) electrical conductivity. High surface area carbon materials include activated carbon, carbon aerogels, carbon nanotubes (CNTs), template porous carbons, and carbon nanofibers [22,59,61,62,87].

Although carbon materials have high surface area, specific capacitance is not directly proportional to their specific surface area. Therefore, many methods have been investigated to functionalized carbon materials by heating treatment, alkaline treatment, steam or CO_2 activation [63,65,67,68]. According to these methods, all kinds of functional groups and heteroatoms can be attached on the surface of carbon materials, which can help the adsorption of ions, so that improve the capacitance of supercapacitor.

Conducting polymers (CPs)

Conducting polymers can be considered as electrode materials mainly because of its outstanding properties, such as, low cost, low environment impact, high voltage window, high storage capacity, excellent conductivity in a doped state, and good reversibility[87]. Conducting polymers have been suggested and investigated for many years[18,58,80,82,84,85,87–89]. During charging and discharging process of CPs based supercapacitor, redox behavior plays an important role to contribute capacitance. Ions are transferred into the polymer backbone when oxidation takes place. In contrast, ions go back into the electrolyte from the backbone when the reduction occurs. These reactions do not include any structural alterations, therefore, the charging and discharging processes are highly reversible and stable[87].

As for CPs, researchers defined the oxidation and reduction processes as "doping" process[58]. One type is "p-doped" polymers, which means oxidation process happens on the repeating units of positively-charged polymers. Another type is "n-type", which means negatively-charged polymers introduced by reduction process.

There are three configurations of CPs supercapacitor[58] .

(1) P-P supercapacitor, in which both electrodes use the same p-dope polymers. After the supercapacitor is fully charged, one electrode is in the full p-doped (positive) stated, and the other is in the uncharged (negative) state.

(2) P-P' supercapacitor, in which electrodes use the different p-dope polymers. Supercapacitor can be charged up due to the different range of oxidation and reduction electroactivities for the two different electrodes

(3) N-P supercapacitor, in which electrodes still use the same polymers, but which can be both n-dope and p-dope in the same unit. Table 1.4 show the types of some key CPs materials normally included PPy, PANI, PTh, and PEDOT

(4) Table 1.4 Types of some normal CPs

CPs-based composites	p-doped	n-doped	n and p doped
polypyrrol (PPy)			
polyaniline (PANI)			
Polythiophene (PTh)			
poly(3,4-ethylene-dioxythiophene) (PEDOT)			

Metal Oxide

Practically speaking, metal oxides can offer higher energy density for supercapacitor than conventional car bon based materials and provide better electrochemical stability when capered with CPs[87]. Generally, the metal should exist in two or more oxidation states that contribute to a continuous range of oxidation reaction with no phase changes involved. Until now, some metal oxides that have been investigated include ruthenium oxide, manganese oxide, cobalt oxide, nickel oxide, and vanadium oxide. The redox reactions of some metal oxide materials are listed below [17,70,72–75]:

1.3.5 Electrochemical properties measurement

There are two electrochemical measurement systems. One is three-electrode configuration system, which is mainly used to measure a single electrode The three electrodes consist of work electrode, counter electrode (graphite rod or Pt foil) and typical reference electrode (Ag/AgCl or Hg/HgO). The other one is two-electrode configurations system, which is used for measuring a supercapacitor device. During measurement, the counter electrode and the reference electrode are connected to the negative electrode of the device, and the work electrode is connected to the positive electrode of the device.

Cyclic voltammetry (CV)

Electrochemical cyclic voltammetry (CV) is a way to record cyclic voltammograms of the device or electrode material, from which the volumetric capacitance and areal capacitance can be calculated by the equation 1.12 and 1.13

where is Volumetric capacitance, is areal capacitance, is the charge, is the potential window, is the volume of the single electrode or the device. is the area of a single electrode or the device.

Galvanostatic Charge-Discharge measurement (GCD)

Galvanostatic charge and discharge measurement (GCD) was performed under a constant current for the charging and discharging process. According to GCD curve, volumetric capacitance and areal capacitance can be calculated by the equation 1.14 and 1.15.

where is Volumetric capacitance, is areal capacitance, is the discharge time, is the operating window, is the volume of the single electrode or the device, and is the area of a single electrode or the device.

Advantages of supercapacitor

Compared to batteries, supercapacitor has several advantages as shown in Table 1.5

(1) High power density.

Supercapacitors display a much higher power density (1-10 kW/kg) than that of lithium ion battery (150 W/kg) review of supercapacitor, which decided by the different charge-discharge mechanism between supercapacitor and battery[49,52]. Supercapacitor stores electrical charge on the surface of electrodes or near the surface, while battery charge-discharge reaction must happen within the entire electrodes. Therefore, the charge-discharge rates of supercapacitor are much faster than the redox reaction inside the electrodes of batteries. Thus, rapid storage rates lead t high power density of supercapacitor.

(2) Long life cycles

Battery stores energy through irreversible faradic reactions between active chemical reagents on the electrodes and ions in the electrolyte. Once all the chemicals are depleted, the reactions stop and the battery is invalid. In contrast, EDLS stored energy purely depends on the physical charge accumulation at the interface. The energy stored in pseudocapacitor is based on reversible chemical reaction during charging and discharging process. Therefore, supercapacitor does not destroy any element during their lifetime and can withstand a huge number of charge-discharge cycles, up to 1,000,000 [52]. Such long-cycling life is impossible for batteries.

(3) Environmental friendly

Supercapacitor do not contain toxic and hazardous materials, and the waste materials are easily disposed.

(4) Wide range of operating temperature

Supercapacitors are function normally at extremely wide range of temperature (from

-40 to 60 ℃) (source from http://batteryuniversity.com/). This is an excellent priority for military applications.

(5) Safety

Supercapacitor are much safer than Li-ion batteries. Explosion will not occur in supercapacitor.

Table 1.5 Comparison of supercapacitor and Li-ion battery (Table source from Courtesy of Maxwell Technology)

Function	**Supercapacitor**	**Lithium-ion battery**
Charging time	1-10 seconds	10-60 minutes
Cycle life	1 million or 30,000h	500 and higher
Cell voltage	2.3 to 2.75 V	3.6 to 3.7 V
Energy density (Wh/kg)	5 (typical)	100-200
Power density (W/kg)	Up to 10,000	150
Cost per Wh	$20 (typical)	$2 (typical)
Service life (in vehicle)	10 to 50 years	5 to 10 years
Operation temperature	-40 to 60 ℃	0 to 45 ℃

1.4 Transparent electrodes for solar cell

Solar energy have great potential to relief energy crises and replace fossil fuels because of its abundance, widespread, environmental friendly properties. Solar cell convert solar energy into electricity and can be applied in various applications. The efforts to reduce the cost of fabrication and to improve the efficiency of solar cells have been a major concern for decades. Optimizing the properties of each element provides an insight to improve their efficiency.

Transparent conducting electrodes with common element of transparent to visible light and good electrical conductivity are essential components for solar cell. Over the last decades, there has a persistent increase in demanding on transparent conducting layers, and there is a continued trend toward flexible and wearable devices, so that the conducting layers need to cater the requirement of these devices [90–101].

Among these applications, solar cell is an important renewable energy technology, which convert sunlight into electricity[93,96]. The amount of solar energy absorbed by Earth’s atmosphere in one hour is more than the total energy consumed in one year [102]. Due to the great potential of solar power, lots of research interests have been attracted in view of its scientific and technical aspects. In order to boost the efficiency of solar power conversion, great efforts have been made to improve the solar energy materials, and solar photovoltaic manufacturing. Transparent electrodes as one important part for solar cell, have attracted enormous research attention with exponentially growing publications[91,93–98,101,103–108].

Traditionally, the transparent conductors have been well served by doped metal oxide, such as indium tin oxide, which has been studied and refined for over years due to its excellent electronic performances [23,109]. However, indium has some unavoidable drawbacks, mainly concentrated on its ceramic nature (the brittle properties result in easily to be damaged), and its low abundance (the limit supply leads to dramatic price fluctuation in industry). Thus, developments in nano-materials research have opened the door for the alternative materials of transparent conducting electrodes.

One of the most mature of these new materials is conductive polymers, such as Poly(3,4-ethylenedioxythiphene)poly(styrenesulfonate) (PEDOT:PSS) [107,110–113]. There also attracted numerous research interests, which focused on carbon-based nanostructure materials, including carbon nanotubes (CNTs) [96,97,107,114,115], and graphene [91,116–118]. Instead, another one of the most important alternative strategy is conductive materials. Ag nanowires (Ag NWs) have recently been attracted a lot of attention for potential application on transparent and flexible electrodes due to the high conductivity of silver [119–125]. Electrical conductivity and optical transparency are the two key properties that usually used to measure the transparent conducting electrode materials. Fig. 1.15 shows the comprehensive comparison of different alternatives of materials through the plot of sheet resistance with respect to transmittance [126]. Each of candidate materials has fundamental advantages and limits as transparent electrodes. Ag NWs demonstrated the best performance with 10 □$^{-1}$ at T=90%, 20 □$^{-1}$ at T=93%, 30 □$^{-1}$ at T=95%, respectively. This performance is comparable to the state-of-art ITO based device, and superior to other alternatives of transparent electrodes, such as graphene, CNT, Ag grid, and thin metal films.

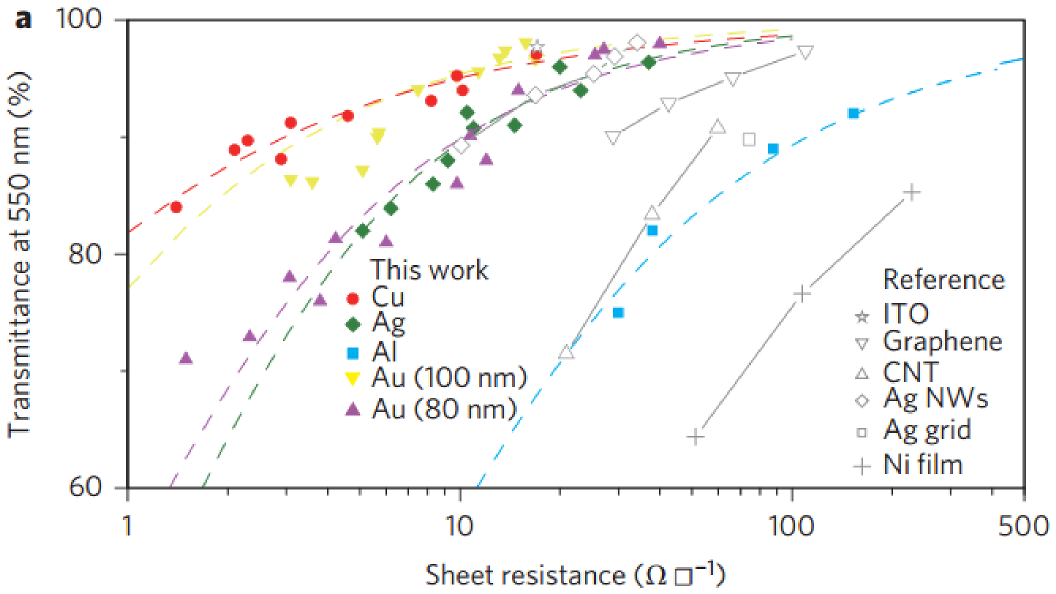

Fig. 1.15 Optical transmittance (at 550 nm) versus sheet resistance for different common transparent conductors [126].

1.5 Motivations and Objectives of this Project

Based on the literature review with respect to energy conversion/storage devices and transparent conducting films, we can find there has been an ever increasing and urgent demand for exploiting sustainable and clean energy nowadays, which give rise to address the rapidly developed worldwide energy crisis.

A series hybrid energy harvest/storage devices directly combine piezoelectric nanogenerator and lithium-ion battery into an integrated one. The novel design can greatly avoid the waste of ambient energy by converting and simultaneously storing mechanical energy directly as electrochemical energy. However, most of these designs are based on battery rather than supercapacitor. Due to the nature properties of supercapacitor, such as higher charging-discharging rate, better cyclability, and higher power density when compared with battery, hence it can be easily concluded that if we utilize supercapacitor as energy storage part, much more significant properties of supercapacitor can be expected to be realized or enhanced the practice range of the novel hybrid devices. Therefore, one of objectives of this thesis is to demonstrate a hybrid piezo-supercapacitor integrated device, which consists of functionalized carbon cloth as the supercapacitor electrodes, and PVDF film as the separator and energy harvester. The mechanical properties and electrochemical properties of the device will be investigated experimentally and theoretically.

Transparent conductive electrode is one of pervasive and essential component for any optoelectronic devices, where light and electricity are synergetic together. Doped metal oxide, such as indium tin oxide (ITO) have already served for this field for almost 60 years [109], but this type of materials have the drawbacks, such as brittleness and high manufacturing cost. In the following, conducive polymer has potential to solve some problems inherent to doped metal oxide, which is usually flexible and easy of produce. However, it always suffers from low environmental stability. Polymer is very sensitive to the change of temperature. Thus, carbon-based material finds opportunity to be widely used in all manner of flexible devices. At the same time, metallic nanowires are especially promising candidate for transparent conducting film, because of its high conductivity. Silver nanowires (AgNWs) have attracted extensive attention for its bendable, high conductivity properties. However, some challenges for the commercialized AgNWs are the complicated fabrication process (need high temperature annealing), and high junction resistance (the high junction resistance is due to the length of Ag NWs usually too short, which increase the density of junctions, so that increase its resistance). Hence, another objective of the study is to synthesize ultro-long Ag NWs, also called Ag nanofibers (Ag NFs) with lower junction resistance and higher transmittance, PVDF/$SnCl_2$ nanofibers were first synthesized by electrospinning technology onto Polyethylene Terephthalate (PET) substrates, followed by deposition Ag nanoparticles on the nanofiber with electroless metal deposition method. The fabrication processes are scalable and takes place at ambient temperature and pressure.

1.6 Scope of the thesis

This thesis is organized as follows:

Chapter 1 is mainly about literature review, which gives a brief introduction on the technologies of energy harvester, energy storage, and hybrid energy harvester/storage device. In addition, a succinct introduction about transparent conducting electrode is included in this part.

In Chapter 2, we demonstrate a rectification-free hybrid piezo-supercapacitor. In this device, externally mechanical impacts establish a piezoelectric potential across the PVDF films, and drive ions in the electrolyte to migrate towards the interface of the supercapacitor electrodes, storing the electricity in the form of electrochemical energy. The detailed fabrication processes, the results of mechanical and electrochemical properties of the device are comprehensively analyzed in this chapter.

In Chapter 3, Ag NFs with promising sheet resistance *Rs* and good transmittance *T* performance was fabricated by combining electrospinning technology and electroless dopsition method. The parameters of electrospinning PVDF/$SnCl_2$ nanofibers were systematically investigated and analyzed. One group of optimum parameters was chosen for the following metallization process. The result of resistance and transmittance of the Ag NFs was measured and discussed in this chapter.

In Chapter 4, we give a conclusion of the whole thesis with the principle understanding of the work and the important results and achievements obtained in the current investigation. Also some future perspectives are included in regard to hybrid energy harvester/storage device, as well as transparent conducting electrodes.

Chapter 2

A rectification-free piezo-supercapacitor with a PVDF separator and functionalized carbon cloth electrodes

The integration of energy harvesting and energy storage device not only enables to convert ambient energy into electricity but also provides sustainable power source for various electronic devices and systems. It is highly desirable to improve the integration level and minimize unnecessary energy loss in the power-management circuits between energy harvesting and storage devices. In our work, we integrate a PVDF film into a supercapacitor as both the separator and the energy harvester. The double-sides of the polarized PVDF films are coated with H_2SO_4/poly(vinyl alcohol) (PVA) gel electrolyte. Functionalized carbon cloths are assembled with H_2SO_4/PVA electrolyte as both anode and cathode, forming a flexible all-solid-state supercapacitor. Externally mechanical impacts establish a piezoelectric potential across the PVDF films, and drive ions in the electrolyte to migrate towards the interface of the supercapacitor electrode, storing the electricity in the form of electrochemical energy. The asymmetric output characteristics of the piezoelectric PVDF film under mechanical impact results in the effective charging of the supercapacitor without any rectification device. The integrated piezo-supercapacitor shows the specific capacitance of 357.6 F/m^2, the power density of 49.67 mWh/m^2, and the energy density of 400 mW/m^2. Our hybridized energy harvesting and storage device can be further extended for providing sustainable power source of various types of sensors.

2.1 Introduction

With the rapid development and high demanding of portable electronic devices, such as portable electronic papers, cell phones, wearable medical device, bendable displays, there has prompted researchers to investigate and look for flexible, lightweight, and high efficiency energy storage technologies. Therefore, these kinds of SCPC draw a growing number of attentions these decades.

Exploring renewable, sustainable, and green energy source is one of the most significative and challenging works to solve energy crises [127–130]. Energy harvesting and storage devices are becoming a key issue for the rapid developments of the energy system [4–8,11,12]. Energy harvesting device can convert the energy in other forms into the electricity but has limited energy storage. Usually, energy harvesting and storage devices are connected together by a power management circuit to enable sustainable power supply [30,33,34,37,131–136]. Piezoelectric materials can convert ubiquitously irregular and low-frequency mechanical vibration into electricity and have been extensively studied for the use of nanogenerator [39,137–144]. Owing to the excellent piezoelectricity and mechanical flexibility, poly-vinylidene fluoride (PVDF) film has been shown for the wearable and flexible energy generator[28–31,33,34,37–40,134].

For the integration of energy harvesting and storage devices, it is important to accumulate and store the harvested energy until a sufficient amount energy can be utilized for electronic devices and systems. In general, a full wave rectifier is used between the piezoelectric nanogenerator and the energy storage device, which decreases integration density and increases unnecessary energy loss. Recently, the self-charging power cell for one-step energy conversion and storage has been demonstrated with the integration of piezoelectric separator and Li-ion battery [145–147]. Xue *et al.* first introduced the fundamental mechanism of hybridizing the two processes into one. Their device is based on combine a piezoelectric nanogenerator and a Li-ion battery, as shown in Fig. 2.1 [146]. The self-charging power cell (SCPC) consists of three major components: anode, cathode, and separator. Aligned TiO_2

nanotebe arrays work as anode. The mixture of $LiCoO_2$/conductive carbon/binder on aluminum foils is regarded as cathode. In addition, a layer of polarized PVDF film, which was located between the two electrodes as the separator and piezoelectric nanogenerator. This device can be charged up by continuous deformation and vibration from the environment.

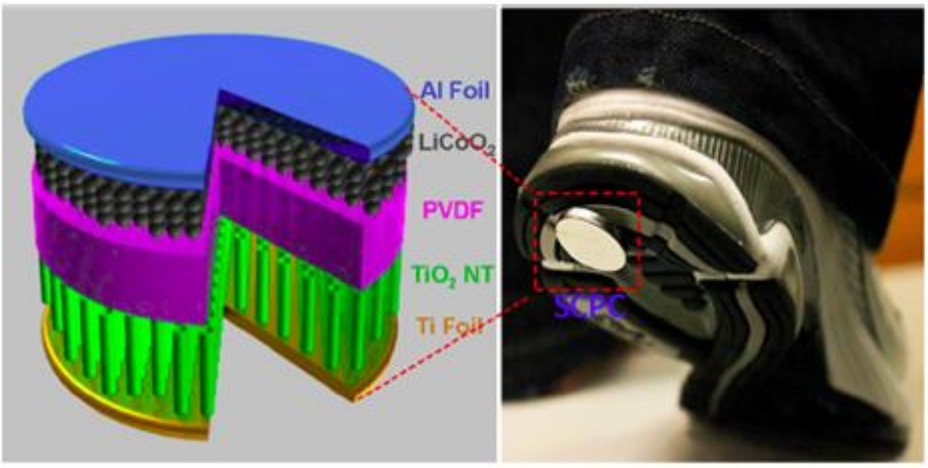

Fig. 2.1 Schematic of first self-charging power cell structure[146]

Xing *et al.* investigated and fabricated the other SCPC by using piezoelectric material to replace the traditional separator of Li-ion battery. In their design, they demonstrated a porous structure of PVDF separator by a template method, as shown in Fig. 2.2 [145]. The SCPC is composed of three important components: anode (grapite/conductive carbon/binder mixture), cathode ($LiCoO_2$/conductive carbon/binder mixture), and a porous PVDF as separator. When compressive stress is applied on the device, a piezoelectric potential is created in the surface of the well-polarized mesoporous PVDF separator, which trigger the migration of Li ion between the cathode and anode.

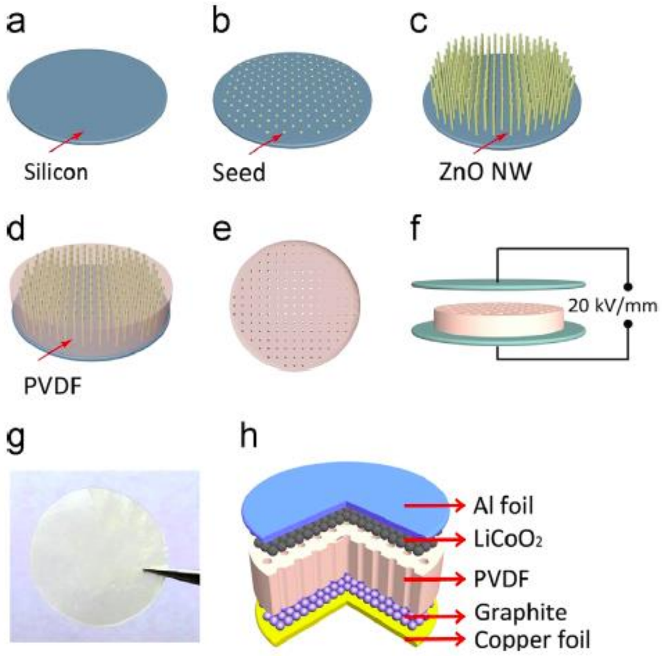

Fig. 2.2 Fabrication process of mesoporous PVDF film by using ZnO nanowire arrays as template and the structure of integrated SCPC.[145]

However, the Li-ion battery is usually limited by slow charging and poor cyclibility. Supercapacitor has gained immense attention as an effective energy storage device due to its higher charging rate, better cyclibility and higher power-density[18,39–42]. More recently, Ramadoss *et al.* have shown the integration of a pesuodo- supercapacitor and piezoelectric materials as a hybrid energy harvesting and storage device[140].

In this work, we demonstrate a hybrid piezo-supercapacitor involving the integration of both energy harvesting and storage. Our device consists of functionalized carbon cloth as the supercapacitor electrodes, PVDF film as the separator and energy harvester, and solid-state PVA as electrolyte. A polarized PVDF film is sandwiched between the symmetric carbon cloth electrodes and electrolyte. Externally mechanical impact establishes a piezoelectric potential across the PVDF film, which serves as a driving force for the migration of ions towards the interface of functionalized carbon cloth electrodes and stores the electricity in the form of electrochemical energy.

2.2 Working mechanism of the hybrid piezo-supercapacitor

PVDF is widely investigated due to its excellent mechanical flexibility and high piezoelectric constant. The β phase PVDF exhibits remarkably piezoelectric properties [44]. The working mechanism of the piezo-supercapacitor is shown in Fig. 2.3. At the beginning, the piezoelectric PVDF film is sandwiched between symmetric FCC electrodes, and surrounded with PVA/H_2SO_4 electrolyte, as shown in Fig. 2.3. (a). It is noteworthy that the free-standing supercapacitor piezoelectric PVDF has an initial voltage of 60 ~ 90 mV instead of zero potential. This initial voltage is possibly caused by the remnant polarization of the PVDF film, which can be induced by the polling process or further increased by compressive stress during the fabrication process. When the electrolyte is intimately contacted with the PVDF film, the charge will be electrostatically induced by the remnant polarization at the interface between the electrolyte and the PVDF. When the piezo-supercapacitor is subjected to a periodic compressive stress, the remnant polarization of the PVDF film is changed, as shown in Fig. 2.3 (b). To balance the changed remnant polarization, charge carriers will be drifted towards the electrode of the supercapacitor. Two factors affect the charging process. First, the increased bonded charge density of the PVDF surface influences the distribution of the positive ions and negative ions in electrolyte. The piezo-potential gives rise to the redistribution of the ions and accumulates the charges on the surface of supercapacitor electrode. Second, the piezo-potential will drive the migration hydrogen ion (H^+) and SO_4^{2-} along the direction of the potential across the porous PVDF film [140,147]. With the increase of the potential between the positive and negative electrodes, more electricity is stored on the electrodes in the form of electrochemical energy. After the H^+ ions and SO_4^{2-} ions redistribute in the electrolyte and balance the piezoelectric field in the PVDF film, the non-faradic and faradic force of the two electrodes reach a new equilibrium, as schematically shown in Fig. 2.3 (c). When the applied compressive stress is released, one self-charging cycle is completed. Fig. 2.3 (d) shows the schematic of the piezo-supercapacitor is under the relaxation stage. A reversed piezoelectric filed was created when the compressive force removed, but the value of the magnitude of this reversed electric-field is around 2 times smaller than that created during compressive process, because the stain rate in the relaxation process is smaller than that in compressive process. Therefore, the reversed piezoelectric field cannot counteract the overall charging process. Thus, the hybrid piezo-supercapacitor can be successfully charged as long as the frequency of the mechanical vibration is larger than a critical value. It is true that the reversed electric-field degrades the energy conversion efficiency of the integrated device. But the elimination of the use of rectification part greatly enhances the integration level of the energy harvesting/storage system. When the device is mechanically deformed again, the process presented above is repeated.

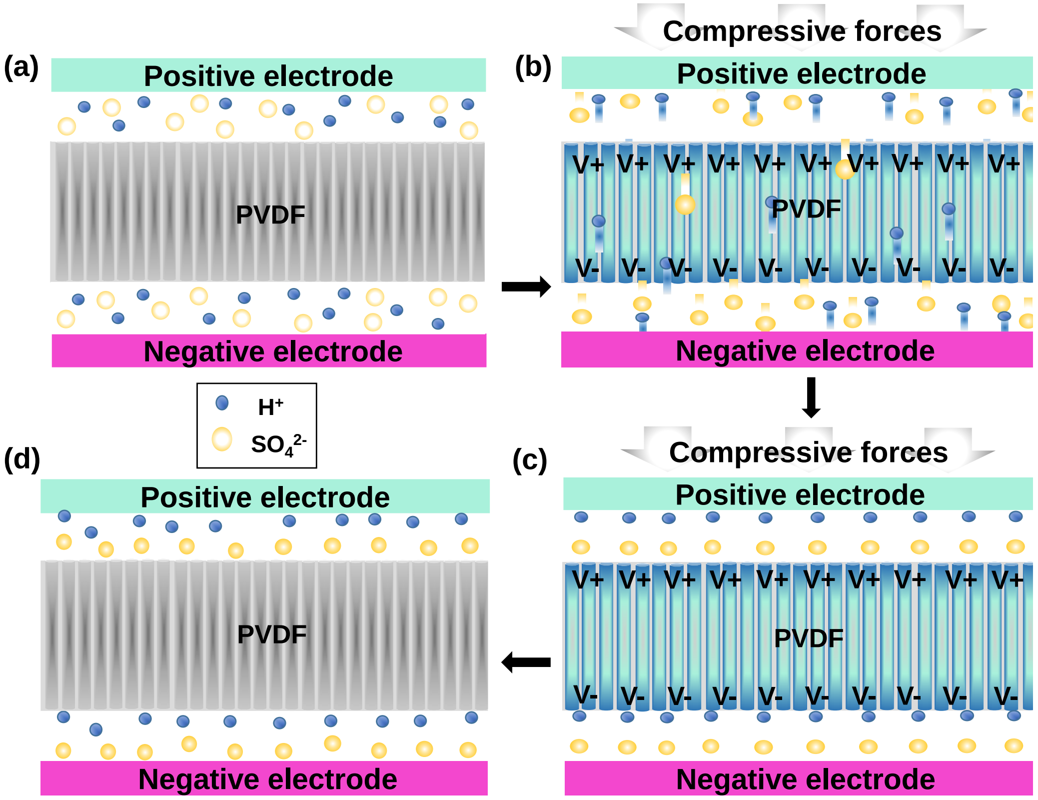

Fig. 2.3. Proposed working mechanism of the hybrid piezo-supercapacitor. (a) Original condition after the fabrication process. (b) The device is under compressive stress. PVDF film creates a piezoelectric field drive the migration of ions. (c) A new equilibrium state is reached between electrochemical and piezoelectric potential. (d) Completed one self-charging cycle.

2.3 Experimental section

2.3.1 Fabrication of the Poly vinyl alcohol (PVA)/H_2SO_4 electrolyte

PVA/H_2SO_4 electrolyte was prepared by mixing concentrated H_2SO_4, PVA powder and deionized water. A 3 g PVA powder (average molecular weight 130,000, Aldrich Chemistry) and 30 mL deionized water were mixed under 90 °C by constant stirring until a homogeneous solution was formed. After cooling down to room temperature, 3 g concentrated H_2SO_4 (97% Analytical grade) was added to the viscous solution.

2.3.2 Fabrication of the functionalized carbon cloth electrodes

Carbon cloth () was purchased from Fuel Cell Earth LLC as the supercapacitor electrode. The carbon cloth was cleaned and dried at room temperature in air. The detailed procedures of preparing the functionalized carbon cloth have been described elsewhere [149]. Briefly, it was functionalized by an anodic electrochemical method with a three-electrode cell system (a piece of carbon cloth with the area of 1.5 cm^2 as the working electrode, a graphite rod as the counter electrode and an Hg/Hg_2Cl_2 as the reference electrode). A voltage of 2.2 V was applied during the electrochemical process for 20 min in a 1M H_2SO_4 solution. The treated carbon cloth was subsequently cleaned by deionized water for several times and annealed in air at 200 °C for 3 hours.

2.3.3 Fabrication of the flexible piezo-supercapacitor

Polarized polyvinylidene fluoride (PVDF) films with a thickness of 100 μm were purchased from Jinzhou KeXin electronic materials Co. Ltd. A piece of PVDF film was cleaned with ethanol by ultrasonic cleaner and used as the separator of the supercapacitor. The PVDF film and two functionalized carbon clothes (FCC) were immersed in the PVA/H_2SO_4 electrolyte for 10 min and dried in air at room temperature. This coating process was repeated for 3 times. The PVDF film coated with PVA/H_2SO_4 was sandwiched between two FCC electrodes to form a symmetrical supercapacitor. The device was dried and solidified in air at room temperature over 8 hours. A supercapacitor without PVDF separator was also fabricated as a control sample.

2.3.4 Characterization

The morphologies of the materials were characterized using a scanning electron microscopy (SEM, JEOL JSM-633F). Raman spectroscopy (HORIBA HR800) with an excitation wavelength of 488 nm was used to measure the vibrational and rotational information about FCC and pure carbon cloth (PCC).The crystalline structures of the

PVDF were investigated using an X-ray diffractometric (XRD, Rigaku Smartlab). The performance of the piezoelectric materials was measured by using an oscilloscope (Agilent Oscillator 3014a). Cyclic voltammetry and galvanostatic charge/discharge were carried out by using an electrochemical workstation (Shanghai Chenhua 660c). The charging/discharging properties of the piezo-supercapacitor were characterized by a Keithely 2410 source meter.

2.4 Result and discussion

2.4.1 Schematic process flow of fabricating the flexible piezo-supercapacitor.

Fig. 2.4 shows the schematic process flow of fabricating the flexible piezo-supercapacitor. We used FCC as the supercapacitor electrode because its excellent mechanical stability and intrinsic flexibility allow it to withstand intensely mechanical vibration. The macroscopic porous structure of the carbon cloth also enhances the intimate contact between the electrodes and electrolytes, which favors the diffusion of ions and the transportation of electrons in the bulk electrode. A simple oxidation and annealing method has been demonstrated as an effective way to introduce various functional groups on the carbon cloth and increase the capacitance by the redox reactions of these functional groups [149]. The PVDF film sandwiched between the two FCC electrodes serves as not only the separator of the supercapacitor but also the piezoelectric energy harvester, which can convert mechanical vibration into electricity. A voltage potential can be generated across the piezoelectric PVDF under externally mechanical vibration. The built-in electric-field across the PVDF film can drive the ions in the electrolyte to migrate towards the interface of the symmetric FCC electrodes, establishing an electronic double layer or pseudo-capacitance at the interface and storing the electricity in the form of electrochemical energy [149].

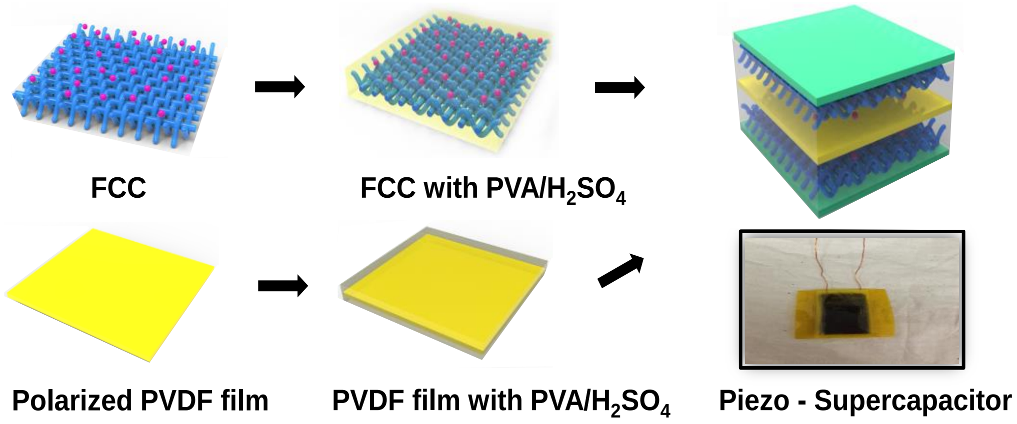

Fig. 2.4 Schematic illustration of the process flow of the hybrid piezo-supercapacitor. PVDF separator and functionalized carbon cloth electrodes are coated with PVA/H_2SO_4 electrolyte, and assembled together.

2.4.2 Structure characterization

Fig. 2.5(a) shows a cross-sectional scanning electron microscopy (SEM) image of the sandwiched structure. The enlarged view in Fig. 2.5(b) shows that the carbon fibers in the electrode are fully surrounded with PVA/H_2SO_4 electrolyte. Fig. 2.5(c) & (d) are the SEM images of the carbon cloth before and after the functionalization, respectively. After the oxidation and annealing processes, a lot of particle-like dots uniformly distributed on the surface of FCC fibers, which were not observed in pure carbon cloth (PCC). We suppose that these are possibly resulted from the carbonyl, hydroxyl, and carboxylic functional groups.

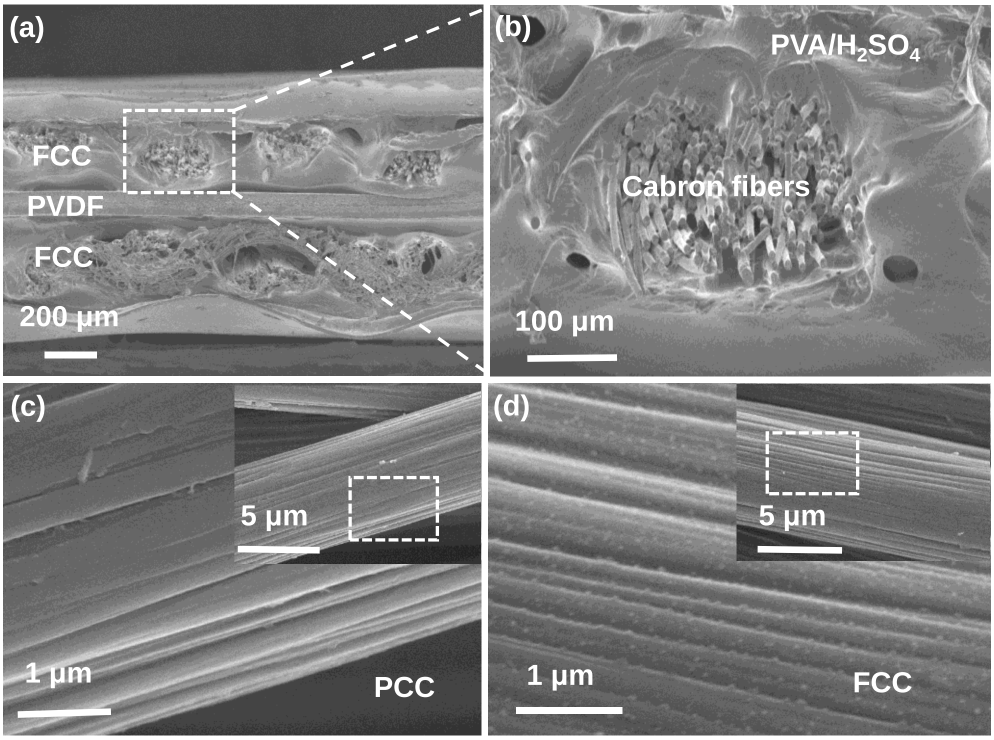

Fig. 2.5 SEM images of (a) the cross section of the piezo-supercapacitor, which consists of symmetric FCC electrodes and piezoelectric PVDF film as a separator and energy harvester. (b) Enlarged view of the functional carbon fibers surrounded by the PVA/H_2SO_4 electrolyte. Enlarged SEM images of (c) the PCC and (d) the FCC. Inset: high-magnification SEM image, which can be seen that the functional groups are attached on the surface of carbon cloth.

In order to further investigate the structure changes in functionalized carbon cloth, we characterized the samples using Raman spectroscopy, as shown in Fig. 2.6(a). The two strong peaks at 1350 cm^{-1} and 1580 cm^{-1} are corresponding to the D band and G band of carbon, respectively. The D band is often referred to the disorder or defect in the carbon, and the G band usually is related to sp^2 carbon-carbon bonding. The table in the inset of Fig. 2.6(a) shows the intensity ratio of D band to G band. The I_D/I_G of the FCC is higher than that of the PCC, indicating that more structural defects are generated in the functionalization process. Fig. 2.6(b) and the insert figures are typical top-view and cross-sectional SEM image of the PVDF film, showing the porous structure. Fig. 2.7 shows the X-ray diffraction (XRD) pattern of the PVDF film. The peak of (1 1 0 / 2 0 0) indicates that the PVDF film is fully polarized β ferroelectric phase.

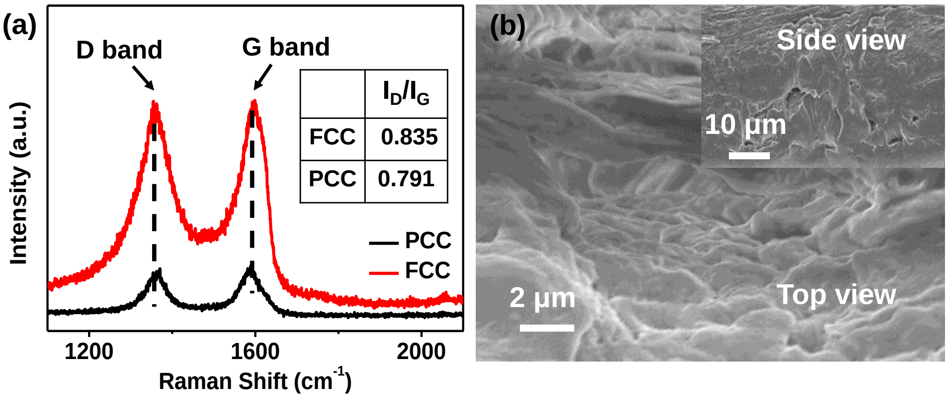

	I_D/I_G
FCC	0.835
PCC	0.791

Fig. 2.6 (a) Raman spectra of FCC and PCC. (b) Top view SEM image of the PVDF film. The inset shows the cross-sectional SEM image.

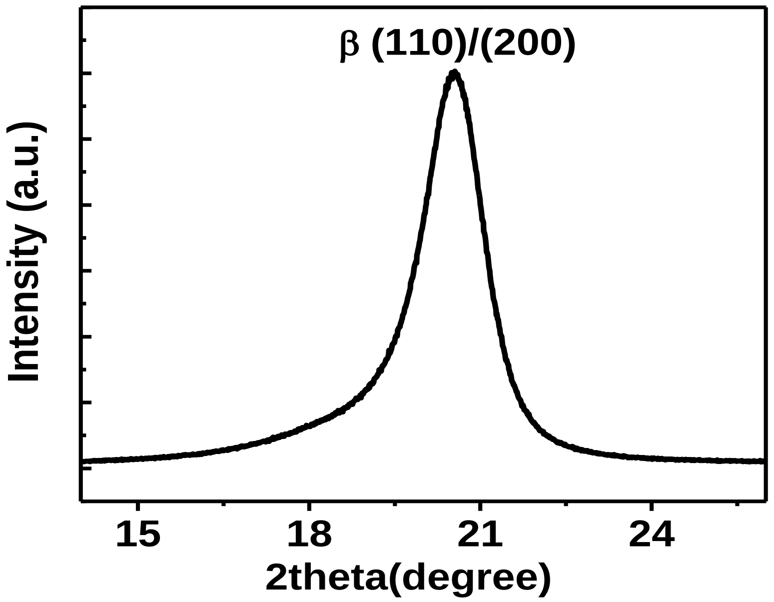

Fig. 2.7 XRD pattern of the PVDF with β-phase (110/200), indicating that the PVDF is fully polarized.

2.4.3 Piezoelectric performance of PVDF

To investigate the piezoelectric performance of the PVDF films, we coated both sides of the polarized PVDF films with an Au layer and measured the output voltage and current. Fig. 2.8 (a) is the output voltage profiles of the PVDF film under a periodic compressive force with average frequency of 4.5 Hz. According to the results, the compressive force produces an output voltage with two opposite polarity peaks. The positive peak corresponds to the stage under compressive forces, while the negative peak represents for the stage of natural relaxation process. The different duration of the two stages gives rise to the asymmetric characteristics of the amplitude in the two peaks, which enables to charge the supercapacitor without a rectification unit. According to the piezoelectricity theory, the generated current of the piezoelectric material under external vibration is proportional to the applied strain rate, as shown in equation [149]:

(2.1)

where Q is the generated charge of piezoelectric generator, t is time duration, d_{33} is the piezoelectric constant, E is the Young's modulus, A is the cross-sectional area, and ε is the applied strain. The strain rate during the relaxation process is relative lower than that during the compressive process by external impact. The generated electric-field in the relaxation process has opposite direction and smaller amplitude compared with the compressive process. Therefore, the charging process is dominated by the compressive process by the mechanical impact. Fig. 2.8 (b) shows the output voltage profile of the PVDF film with the opposite polarization. In addition, the magnitude of the piezoelectric potential is linearly proportional to the magnitude of applied force [145–147]. The intensely mechanical impact will results in strong built-in electric-field.

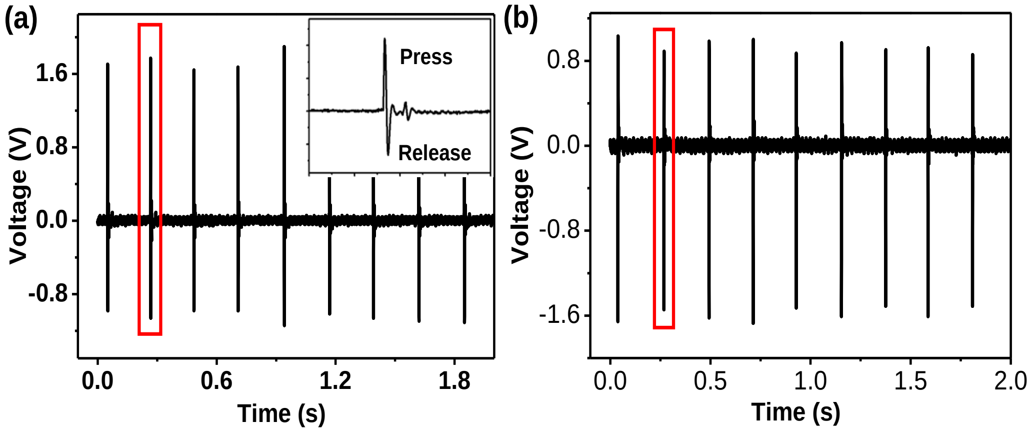

Fig. 2.8 (a) and (b) The voltage output profiles of PVDF separator with opposite polarization under a periodic mechanical compressive straining. Enlarged image of (a) shows the opposite output during once stress applied, which is due to the difference in strain rate of the PVDF film when be compressed and released.

2.4.4 Electrochemical characterization of supercapacitor

Fig. 2.9 shows the cyclic voltammetry (CV) curves of the symmetric supercapacitors with FCC electrodes and PCC electrodes with the sweep rate of 100 mV/s. The CV curve of the supercapacitor with the PCC electrodes shows almost negligible capacitance. The CV curve of the supercapacitor with the FCC electrodes shows rectangular shape within the operation voltage range of 0-1 V, suggesting that the FCC electrode exhibits significant improvement of the capacity. After the functionalization, the areal capacitance of the carbon cloth electrode is increased by 214 times. These results demonstrate that the anodic electrochemical oxidation process is an effective and simple method to increase the capacitance by orders of magnitude of carbon-based electrodes. This outstanding performance of the FCC electrode is mainly ascribed to the Faradaic reaction of these $>$CO, $>$COH and COOH functional group [149]:

$$>\mathrm{COH} \Leftrightarrow\ >\mathrm{CO} + \mathrm{H}^+ + \mathrm{e}^- \tag{2.2}$$

$$\mathrm{COOH} \Leftrightarrow \mathrm{COO} + \mathrm{H}^+ + \mathrm{e}^- \tag{2.3}$$

$$>\mathrm{CO} + \mathrm{e}^- \Leftrightarrow\ >\mathrm{CO}^- \tag{2.4}$$

In addition, the electrochemical performance of the FCC electrodes is also affected by the annealing temperature. With the annealing temperature increased from room temperature to 100 ℃, 200 ℃, and 300 ℃, the amount of the functional groups decreased and the conductivity of FCC was increased. Good electrical conductivity is helpful to achieve high charging/discharging rate. But the decrease of functional groups also reduces the capacity. Thus, the annealing temperature plays an important role to balance the conductivity and the capacity of the supercapacitor electrode. In this work, we used the FCC electrodes annealed at 200 ℃ as the supercapacitor electrode.

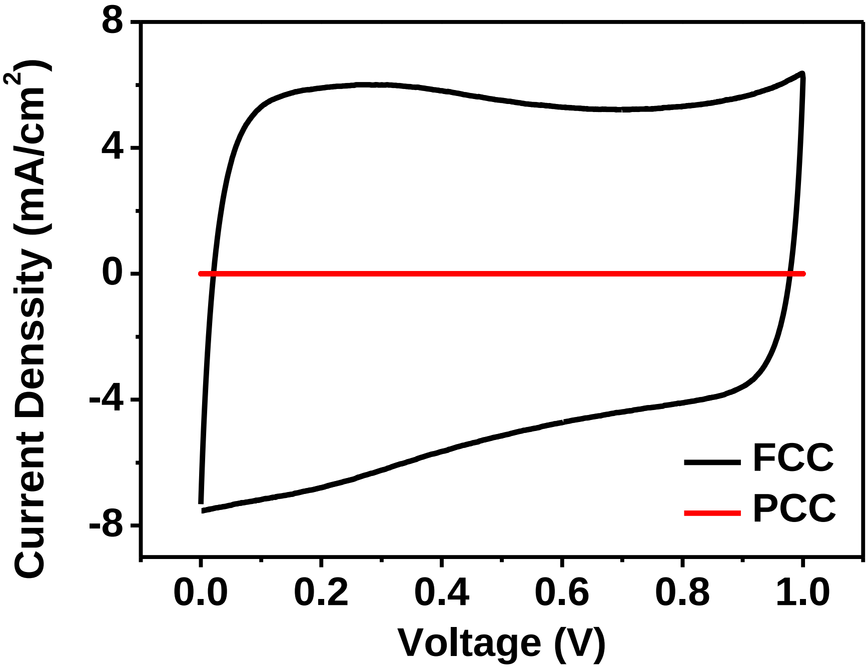

Fig. 2.9 Cyclic voltammograms curves measured at a scan rate of 100 mV/s for the supercapacitor with symmetric PCC and FCC electrodes.

Fig. 2.10 (a) shows the CV curves of the piezo-supercapacitor with the PVDF separator. The shape of the CV curves is quasi-rectangular at different scan rates, ranging between 10 and 500 mV/s, indicating good electrochemical properties of the supercapacitor. Fig. 2.10 (b) shows the galvanostatic charge–discharge (GCD) curves of the piezo-supercapacitor, which was conducted between 0 and 1V at different charge/discharge current densities. The device shows a stable isosceles triangle shape even at high current density, which confirming again an excellent capacitive behavior. Fig. 2.11 (a) shows the CV curves of the supercapacitor without the PVDF separator and exhibits similar behavior with that of the piezo-supercapacitor. The GCD curves of supercapacitor without PVDF separator are shown in Fig. 2.11 (b).

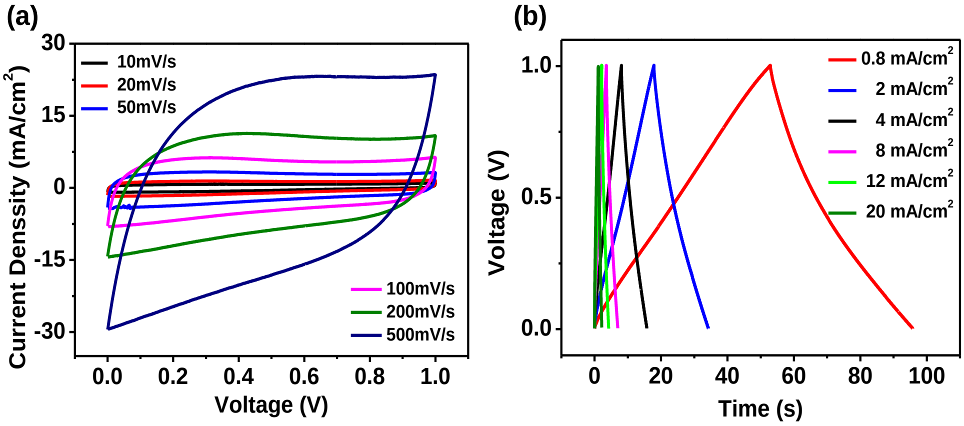

Fig. 2.10 (a) CV curves of the FCC supercapacitor with the PVDF separator measured at scan rates of 10, 20, 50, 100, 200, and 500 mV/s. (b) Galvanostatic charging and discharging curves of the piezo-supercapacitor measured at different current densities from 8 to 200 A/m^2.

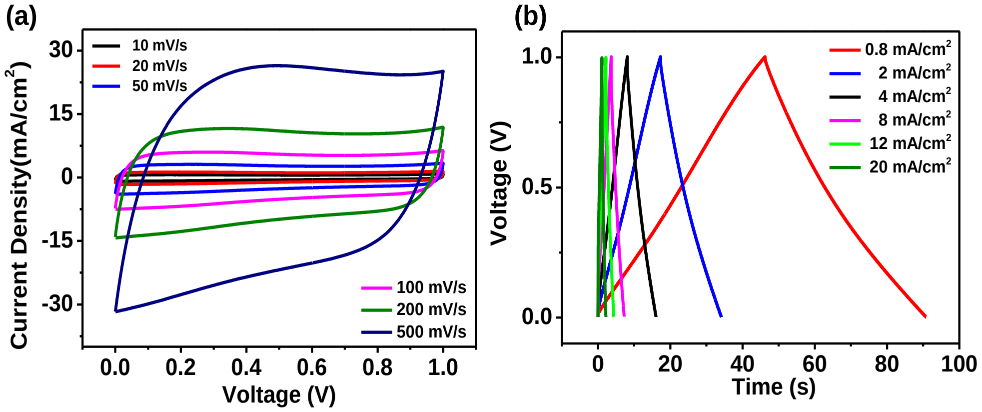

Fig. 2.11 (a) & (b) CV curves and galvanostatic charge and discharge curve of FCC supercapacitor without PVDF separator

The areal capacitance (C_m) of piezo-supercapacitor was calculated according to the equation (2.5):

(2.5)

where C_m is the areal capacitance, is the discharge current, is the discharge time, S is the effective area of the FCC electrodes (~ 1 cm^2), is the potential range during the discharge process. According to Fig. 2.12 (a), the extracted areal capacitances of supercapacitor with PVDF separator are 357.6, 337.2, 318.8, 287.2, 260.4, 214 F/m^2 at the current densities of 8, 20, 40, 80, 100, 120, 200 A/m^2, respectively. The maximum specific capacitance of 357.6 F/m^2 is obtained at the current density of 8 A/m^2. More importantly, it exhibits a relatively good charge/discharge rate capability, retaining 59.84% of the capacitance when the current density increased from 8 to 200

A/m^2. Fig. 2.12 (b) shows the calculated areal capacitance of the supercapacitor with and without the PVDF film. These results suggest that the electrochemical properties of the supercapacitor with the PVDF separator are comparable to those without it. The highest areal energy density *E* of the device calculated based on GCD curve is 49.67 mWh/m^2, and the power density of the device is 400 mW/m^2, indicating comparatively good power output ability. Fig. 2.13 shows the CV curves of the piezo-supercapacitor under different mechanical deformation states (flat, bent and twisted), exhibiting negligible difference and indicating excellent mechanical flexibility.

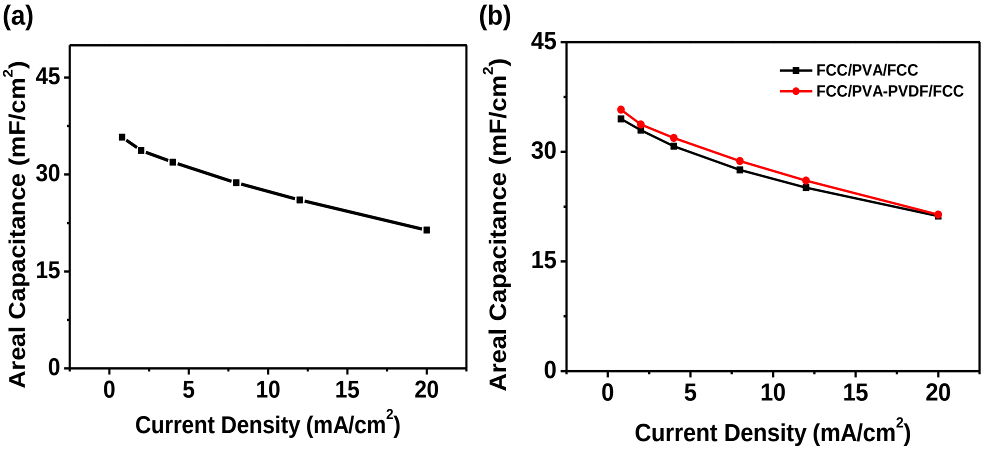

Fig. 2.12 (a) Calculated areal capacitance of the supercapacitor with PVDF separator based on galvanostatic charging-discharging current density. (b) Comparason of calculated areal capacitance of the supercapacitor with and without PVDF separator based on galvanostatic charging-discharging current density.

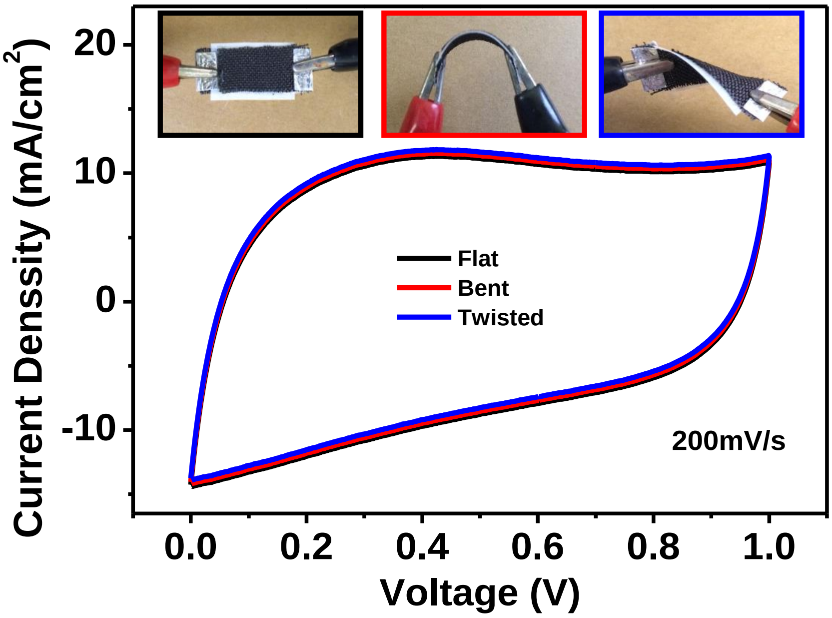

Fig. 2.13 CV curves of supercapacitor in flat, bent and twisted states at a scan rate of 200 mV/s. Insets are the device pictures under different test conditions.

2.4.5 Self-charging performance of piezo-supercapacitor

Fig. 2.14 shows a typical charging process of the piezo-supercapacitor. At first, the initial voltage of the device was discharged to zero under a constant current of 100 μA. After that, the charging process was under a continuous compressive force with the average frequency of 4.5 Hz. Then, the device was discharged at a constant current of 100 μA again. According to these results, the voltage of the supercapacitor was increased to 100 mV within 40 s. Based on the calculation of the discharging curve, the stored electric capacity was about 0.25 μAh. The piezo-supercapacitor showed an areal capacitance of 100 F/m^2, almost 30% of the areal capacitance of supercapacitor which is charged by external power source. The energy density and power density of the piezo-supercapacitor charged by mechanical force are 0.278 mWh/m^2 and 0.028 mW/m^2.

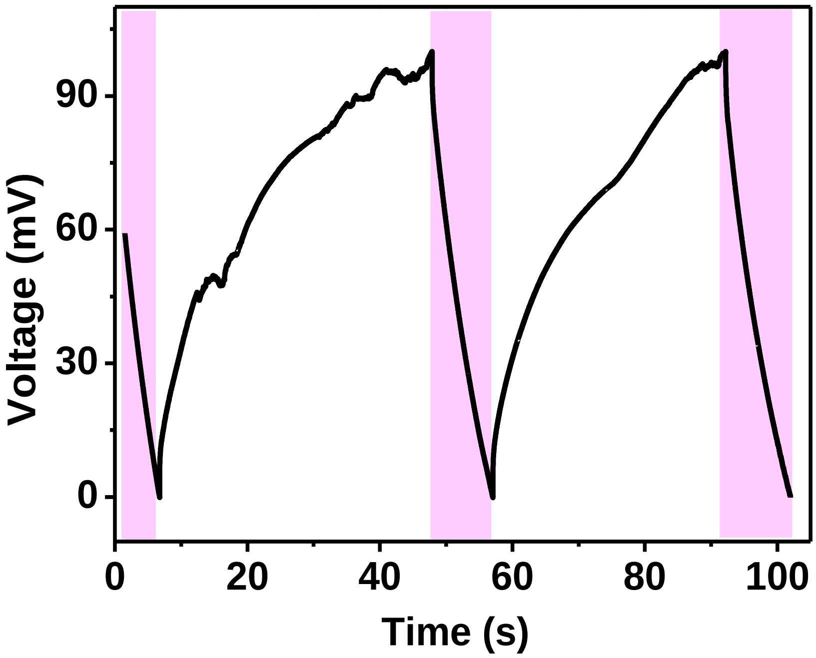

Fig. 2.14 Typical self-charging process performance of a piezo-supercapacitor.

To confirm that the increased voltage of the supercapacitor is resulted from the piezoelectric separator, we replaced the PVDF film with a commonly used separator without piezoelectric properties (NKK TF40, 40 μm thickness) and measured the voltage response under the same periodic force condition. Fig. 2.15 shows the corresponding result. During the stage of the initial 2000 s without any external forces, the device shows the leakage characteristics. In the following 2000 s with a repeated compressive force, the device still keeps the linearly decrease rate and cannot be charged up at all. Therefore, the supercapacitor without piezoelectric separator cannot be charged by applying a repeatable mechanical deformation. This indicates that the charging of the supercapacitor is truly resulted from the piezoelectric PVDF separator.

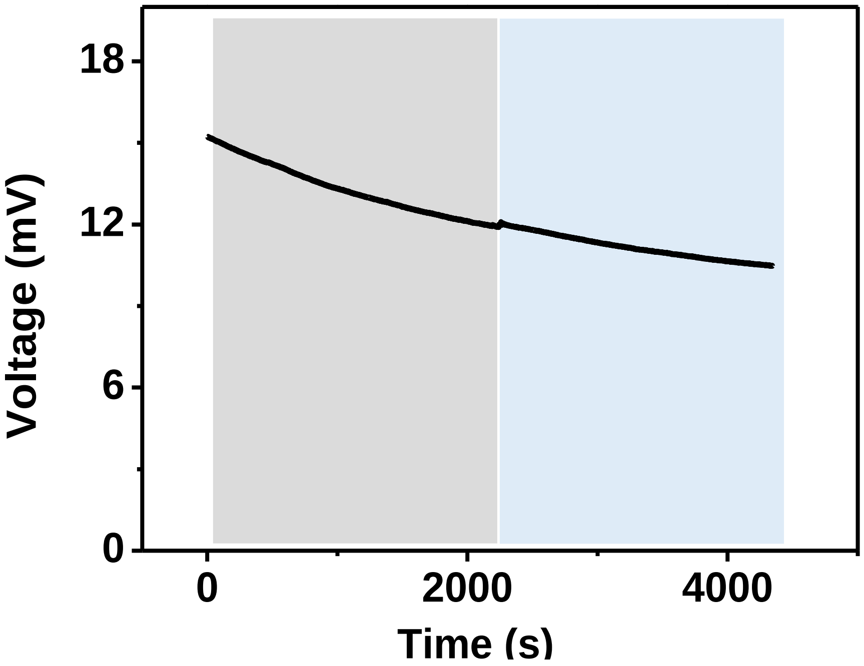

Fig. 2.15 The PVDF separator was replaced with commonly used NKK. No self-charging effect was observed.

2.5 Summary

In summary, we successfully fabricated a rectification-free piezo-supercapacitor, which integrates both supercapacitor and piezoelectric energy harvesting film. The flexible piezoelectric PVDF film can convert mechanical vibration into a built-in electric-field, which serves as the driving force for the migration of ions towards the interface of the FCC electrodes. The asymmetric characteristics of the PVDF film during compress and relaxation stages results in the effective charging without any rectification device. The flexible piezo-supercapacitor exhibits that it can maintain high mechanical strength and high capacitance simultaneously under the bending and stretching test, and shows stable electrochemical performance with energy density 49.67 mWh/m^2 and power density 400 mW/m^2. Our device can be further extended for providing sustainable power source of various types of sensors.

Chapter 3

Transparent Conducting Nanofiber of Electrospun PVDF/$SnCl_2$ with Ag for Electrode Application

Silver nanofibers (Ag NFs) have attracted considerable attention for their potential applications in transparent electrode to replace indium tin oxide (ITO)[152–155]. Herein, an optimized electrospinning method and electroless deposition are combined together to fabricate Ag NFs transparent conducting electrode (TCE). Electrospinning method usually utilized to fabricate ultrolong nanofibers from all classes of materials either directly or indirectly. Based on the outstanding advantages of electrospinning technology, such as the ease of material combination, ease of fiber functionalization, ease of nanofiber deposition onto different substrate, and mass production capability, electrospinning method became the crucial part in this study. The PVDF/$SnCl_2$ nanofibers are fabricated and subsequently employed as template for the following electroless Ag deposition. The morphology and composition of the Ag NFs are systematically analyzed. It shows an excellent conductivity of $73.55\ \Omega\ \square^{-1}$ and $15.35\ \Omega\ \square^{-1}$ (transmittance of 84% and 75%) and maintains its conductive properties even after 100 bending cycles. Importantly, the ratio of electric conductance to optical conductance (), the commonly used figure of merit for transparent conductors, reached to 80 when *Rs* is 15.35 Ω □$^{-1}$ (T = 75%). This is much higher than other transparent electrodes, such as graphene ~ 0.5, and for nanotubes ~ 25 [120]. In addition, this Ag NFs transparent electrode is flexible and shown with good stability, which was fabricated under ambient temperature. Hence, these results and fabrication processes make the thin film a promising replacement for ITO as transparent electrodes, and open the door for large scale production, and meet the huge demanding in industry.

3.1 Introduction

With the unprecedented development of these modern popular electronics, transparent electrodes are receiving extensive attention. Indium tin oxide (ITO) is the most common transparent electrode in these devices due to its high optical transparency (90%) and low sheet resistance (15 Ω □$^{-1}$) [125]. However, ITO has some inherent drawbacks, for example, (1) the ceramic nature makes it easily damaged, which hinders its applications in flexible devices; (2) the scarcity of rare-earth element supply leads it to a high price [23,109], which limit their compatibility with mass production of large-area and low-cost devices. Hence, many researchers have focused on next-generation material to replace ITO[91,96,107,114,116,117,126,156,157]. There are some emerging alternatives, such as, conductive polymers [107,110–113], carbon nanotubes (CNT) [96,97,107,114,115], graphenes [91,116–118], metal grids [106,156,158], metal nanowires[119,122,123,125,159], which have various degrees of success relative to address these issues. However, these materials have their own problems. CNT require strong acid treatment and surfactants, but only yield the transparent films with Rs = 43 Ω $\square^{-1}$, and a transmittance of 89% [124]. Cost associated with graphene is still a negative factor, the high manufacturing cost hinder its applications [91]. The major problem for conductive polymers is the instability of the doped state, which can easily decrease the electronic conductivity during variable mechanical, thermal, chemical environment [23]. Therefore, this instability is the main reason for hindering conductive polymers from widespread applications.

Ag NFs has been demonstrated to be a potentially good transparent conductor due to its comparable transparency and sheet resistance values to that of ITO, ease of fabrication, and low-cost. Different approaches of manufacturing Ag NFs on various substrates have been demonstrated [23,120,122–125,160,161]. Junction resistance of Ag NFs has become the key issue to enhance the performance of Ag NFs transparent electrodes, because this primarily influences the conductivity of Ag NFs [123]. In order to reduce the junction resistance without compromising optical transmittance, a group set of methods have been investigated, such as, thermal annealing [159], nanoplasmonic welding [121], electroelding [162] , and wet chemical coating [163]. Nevertheless, these approaches usually limit the use of substrate and increase the complexity of fabrication processes.

In our work, we propose a novel method, which combines electrospinning technique and electrolessly metal deposition method to synthesize ultra-long and low junction-resistance transparent electrode based on Ag NFs on flexible Polyethylene Terephthalate (PET) substrate. The average diameter of Ag nanofiber is around 258 2 nm, which uniformly distribute on the substrate. The conductive properties are stable even under flexing for at least 100 cycles.

3.2 Experimental process

3.2.1 PVDF/$SnCl_2$ solution preparation

We prepared different concentrations (18wt%/9wt%, 14.1wt%/9.41wt%, and 12wt%/12wt%) of PVDF/$SnCl_2$ in electrospinning solutions to investigate the effects on the morphology. The solvent is N,N-Dimethylformamide (DMF, ACS reagent, 99.8%, Sigma-Aldrich) and Acetone (ACS reagent, 99.5%, Sigma-Aldrich) with the volume ratio 7:3. According to the calculation, $SnCl_2$ (reagent grade, 98%, International laboratory USA) powder was firstly mixed with the solvent by constant stirring. After the homogenous solution was formed, certain amount of Polyvinylidene fluoride (PVDF, average Mw ~ 275,000 by GPC, Sigma-Aldrich) was added to the solution and stirred at for 5 hours until the solution became clear and homogeneous.

3.2.2 Nanofiber synthesis procedures

Commercialized Alumium (Al) foil was used to attach on the collector for electrospinning, then a PET substrate (1.5cm1.5cm100µm, Plastemart.com) was adhered to the Al foil to receive electrospun nanofiber. After fixed the syringe, the flow rate was preset at 0.3 ml/h to the syringe pump. The positive and grounded terminals were connected to the needle and collector, respectively. The voltage was applied to the apparatus within 8 ~ 12 kV. The electrospinning process was conducted for 1~ 7 mins. After stopped the syringe pump and the power supply, the nanofiber template was baked at 85 for12 hours to evaporate the organic solvent.

3.2.3 Electroless deposition

The PVDF/$SnCl_2$ electrospun nanofibers on a PET substrate were immersed into 25 g/L $AgNO_3$ (Acs reagent,99.0%, Sigma-Aldrich) solution for 30 min to grow Ag seed layers. Then, the nanofibers were rinsed by DI water thoroughly. The sample was immersed into vigorously stirring 17.5g/L L-ascorbic acid (Asa, Sinopharm Chemical Reagent Co., Lid) [164]. 5 ml silver-ammonia solution ($Ag(NH_3)_2^+$) was added into Asa dropwisely, Ag^+ was reduced and deposited on nanowires, where the $Ag(NH_3)_2^+$ was used as Ag precursor, which was prepared by adding 2% NH_3H_2O (28% NH_3 in H_2O, ≥99.99% trace metals basis, Sigma-Aldrich) into 5g/L $AgNO_3$ aqueous solution dropwisely until the brown precipitate disappears and the solution becomes clear again.

3.2.4 Measurement and Characterization

For each stage during electrospinning and electroless deposition, the morphologies of the PVDF/$SnCl_2$ nanofibers and Ag NFs were characterized by scanning electron microscopy (SEM, JEOL JSM-633F), scanning transmission electron microscopy (STEM, JEOL JEM-2100F), and X-ray Diffractometer (XRD, Rigaku SmartLab). Meanwhile, the corresponding energy dispersive X-ray spectroscopy (EDX) of the nanofiber with and without deposited Ag particle on the surface were detected based on the nanofiber. The transmittance spectra of the Ag nanofiber were measured by utilizing a UV-Vis spectrophotometer (UV-2550, Shimadzu, Japan) under the wavelength of 300-800 nm. The transmittance spectrum was obtained based on the reference plain PET film. The sheet resistance was measured by using a Four-Point probe test system by using Keithley 2400 and 2410 sourcemeter.

3.3 Result and discussion

3.3.1 Working mechanism of the electroless deposition of Ag

Fig. 3.1 illustrates the procedures to synthesize Ag nanowire transparent conducting electrodes (TCEs) at ambient temperature. A PET acts as the flexible substrate mainly due to its transparency, lightweight, high tensile strength, non-toxic, excellent mechanical stability even at very high temperature [165,166]. First, electrospinning technique was used to fabricate ultra-long PVDF/$SnCl_2$ nanofibers networks on the PET substrate. Second, the nanofiber network worked as a template for the following electroless metallic deposition process. The PVDF/$SnCl_2$ nanofibers was immersed in silver nitrate aqueous solution (25 g/L $AgNO_3$), where Ag^+ was reduced by Sn^{2+}, and exiguous Ag seeds then attached on the fibers to form a catalyst layer. This process (step 1) is an important catalytic reaction to trigger electroless Ag deposition (EAD) [167].The catalyst Ag seeds layer therefore acted as the electron carrier for the following transfer of electrons from the reducing agent Asa to the Ag ions in solutions, and then

Ag particles were covered the whole surface of PVDF/$SnCl_2$ nanofibers and naturally "fuse" the junctions of two nanofibers (This process is called step 2). The detail mechanism of electroless deposition of Ag as shown in Fig. 3.2, and the redox reaction as follows:

Oxidation:

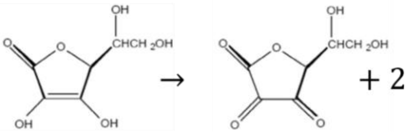

$+ 2\,H^{+} + 2e^{-}$ (3.1)

Reduction： (3.2)

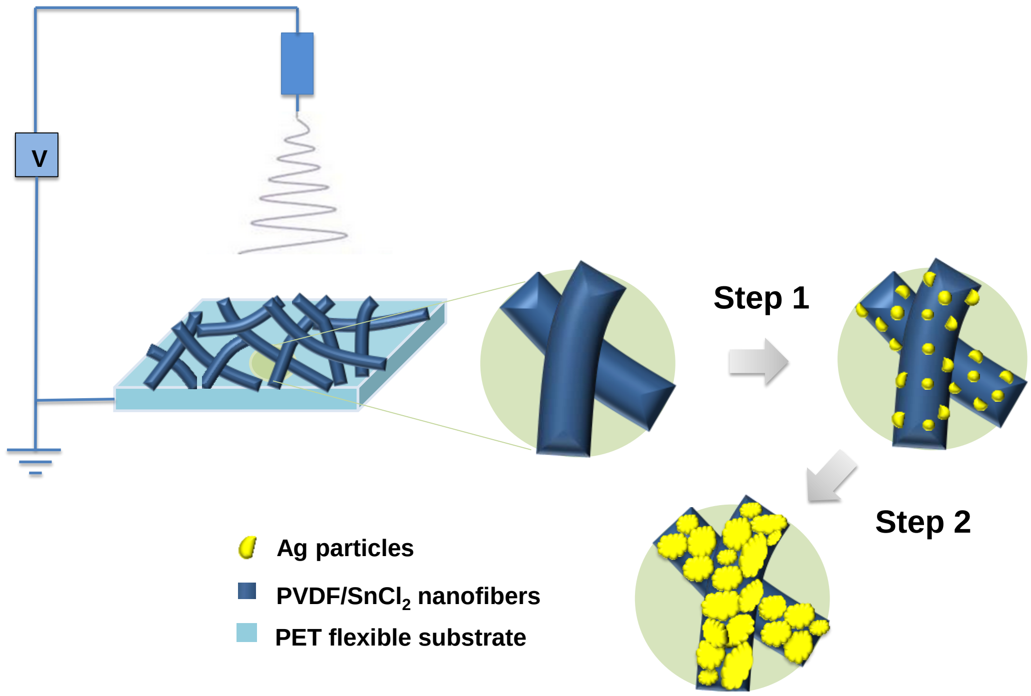

Fig. 3.1 Schematic of synthesis Ag NFs transparent electrode. PVDF/$SnCl_2$ nanofibers were electrspun onto the flexible PET substrate, Ag seed catalyst layer formed in the following. Continuous Ag nanofiber formed finally.

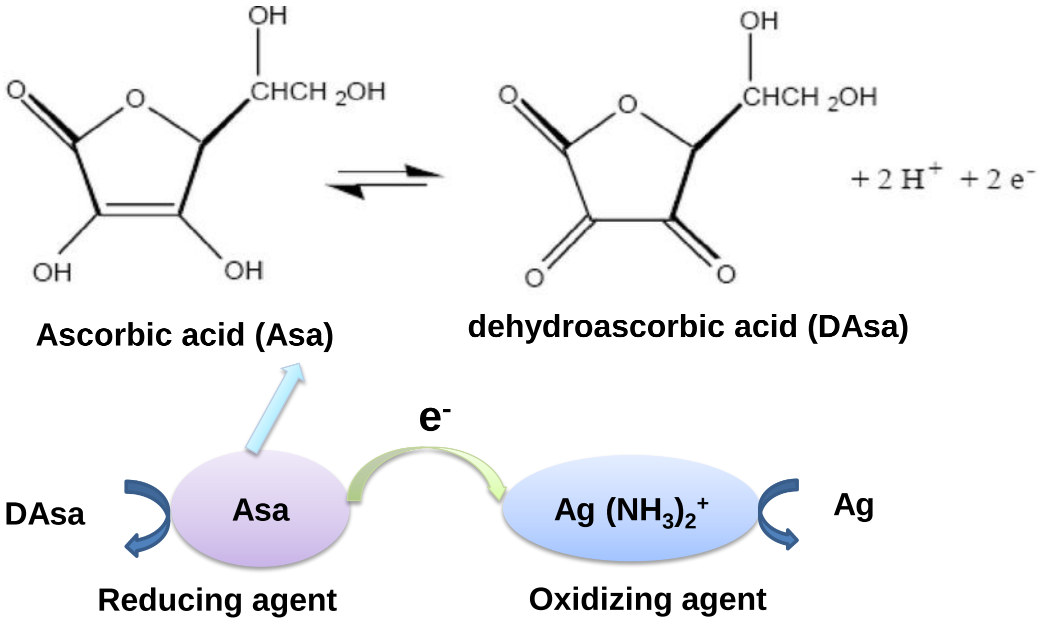

Fig. 3.2 The detailed mechanism of electroless Ag deposition.

3.3.2 Optimizing parameters of electrospining for high quality PVDF/SnCl$_2$ nanofiber

The quality of Ag NFs mainly depends on the precursor PVDF/SnCl$_2$ electrospinning nanofiber. Therefore, optimizing PVDF/SnCl$_2$ plays an important role in the whole study design. The electrospining nanofibers are mainly influenced by the following factors, such as, polymer concentration in solution, applied voltage, and flow rate [168]. In order to fabricate nanofiber with excellent morphology, several experiments have been carried out by changing the parameters mentioned above.

3.3.2.1 Polymer Concentration

Metal salt solution ($SnCl_2$) and polymer solution (PVDF) mixed together to form the electrospinning solution. The solution viscosity significantly influenced by the mass ratio of polymer to metal salt. Table 3.1 documents the three different groups of solutions, which are defined by different mass ratio of PVDF to $SnCl_2$. Fig 3.3 shows the representative optical and SEM images of nanofibers based on the different solutions. The optical image in Fig. 3.3 (a) shows a flocculence cluster attached on the collector, where the mass ratio of PVDF to $SnCl_2$ is 2:1. The viscosity of the solution was too high to spin. It is difficult to push the drop into the sprayers by the syringe pump when the solution with such high concentration of PVDF. Therefore, the solution with lower concentration of polymer PVDF was investigated. Fig. 3.3 (b) and (c) show the SEM images of the electrospun nanofiber prepared with the mass ratio of PVDF and $SnCl_2$ (1.5:1 and 1:1), respectively, where the other parameters of the electrospinning process are kept unchanged. According to the result of SEM image, the fiber based on the mass ratio of 1.5:1 turn out to be more uniform compared with that prepared by the mass ratio of 1:1. In addition, it is relative easier to spin when the mass ratio is 1.5:1. Therefore, on the basis of these findings, the mass ratio of PVDF and $SnCl_2$ (1.5:1) was optimum polymer concentration, which was used in the following experiments.

Table 3.1 Detailed information of three groups of the solutions with different mass ratios of PVDF to $SnCl_2$

	PVDF/$SnCl_2$ concentration	Applied voltage (kV)	Flow rate (ml/h)
PVDF/$SnCl_2$ (a)	18wt%/9wt% (2:1)	8	0.3
PVDF/$SnCl_2$ (b)	14.1wt%/9.41wt% (1.5:1)	8	0.3
PVDF/$SnCl_2$ (c)	12wt%/12wt% (1:1)	8	0.3

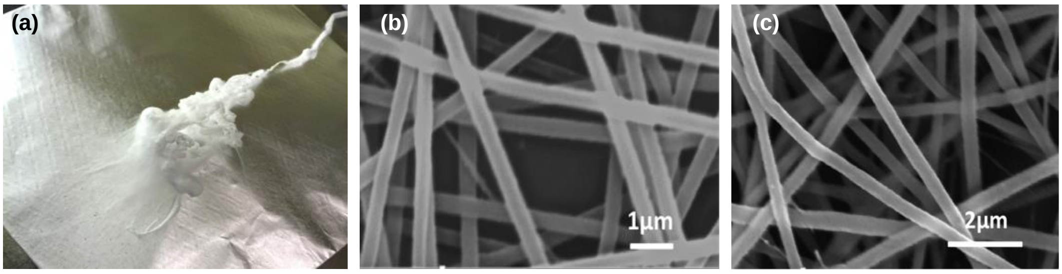

Fig. 3.3 Optical and SEM images of nanofibers based on different PVDF concentration in solution. (a) photonic flocculence nanofibers on the collector prepared by mass ratio of PVDF to $SnCl_2$ with 2:1, (b) and (c) SEM micrographs of electrospun nanofiber prepared by mass ration of PVDF to $SnCl_2$ with 1.5:1 and 1:1, respectively.

3.3.2.2 Applied voltage

Effects of applied voltage on morphology of electrospun nanofibers were investigated. A constant volume of the feeding solution was delivered to the needle at a flow rate of 0.3 ml/h, and a high potentials in the range of 8 kV ~ 12 kV was applied. Fig. 3.4 shows the morphologies of PVDF/$SnCl_2$ nanofibers electrospun with different applied voltages (8 kV, 9 kV, 10 kV, and 12 kV). According to the SEM images, we found that the diameter of nanofibers have no drastic difference under the change of applied voltage from 8 to 10 kV. Therefore, we can adjust the applied voltage within the range of the voltage (8 ~ 10 kV) during actual operation.

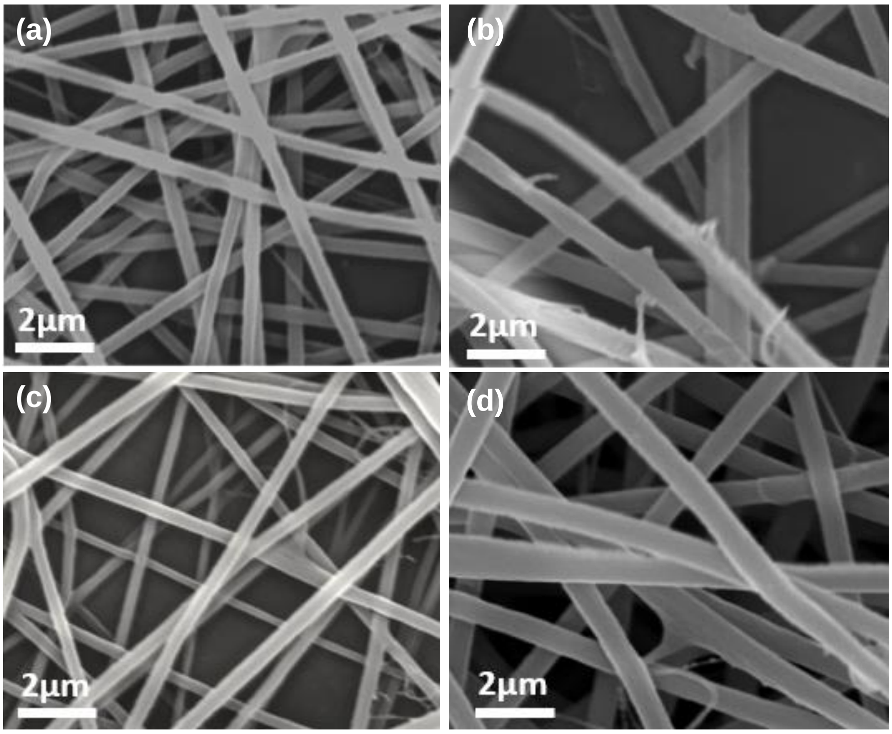

Fig. 3.4 SEM images of PVDF/$SnCl_2$ prepared by different applied voltage. (a) 8 kV, (b) 9 kV, (c) 10 kV, (d) 12 kV.

3.3.3 Comparing the morphology and composition of the nanofiber before and after Ag deposition

Fig. 3.5 (a) shows the SEM image of PVDF/$SnCl_2$ nanofibers. It can be seen that the nanofibers exhibit ultra-fine fibrous morphology. The surface of the nanofibers appears to be uniform. The length of the nanofibers larger than 200 μm as shown in Fig 3.6. The enlarged view in Fig. 3.5(b) shows the junction section of the crossed nanofibers. The boundary of the junction is very clear, and the fiber is on the above another fiber, exhibiting a certain gap distance. Fig. 3.5(e) shows the corresponding histogram of nanofibers diameter distribution analysis, which reveals that the average nanofibers diameter is about 261 3 nm.

Fig. 3.5(c) shows the SEM image of nanofibers after the electroless Ag deposition process. Lots of particle-like things are distributed on the surface of the nanofibers. We characterized the particle things on nanofibers by using XRD and TEM measurement following. Fig. 3.5 (d) shows the magnified view of the junction of the nanofibers. It can be seen that the junction of the two separated nanofibers almost be “fused” by Ag. The boundary of each fiber in the junction part was connected together. This feature helps to reduce the junction resistance for the Ag NFs thin film. Fig. 3.5 (f) shows the diameter distribution of Ag NFs. The nanofiber diameter shows negligible change before and after Ag deposition. The average diameter is 258 2 nm. The average diameter of the Ag coated NFs shows insignificant, or even smaller than that of the uncoated nanofiber. This might because some organic solvent still exists in PVDF/SnCl2 nanofibers before Ag deposition. The subsequently electroless metallic deposition process is carried out in solution. The organic solvent in nanofibers could be dissolved in the solution for electroless deposition. Although Ag is coated on the surface of nanofibers, there is also mass loss during the electroless process. Therefore, the diameter for Ag-coated NFs exhibits insignificant change.

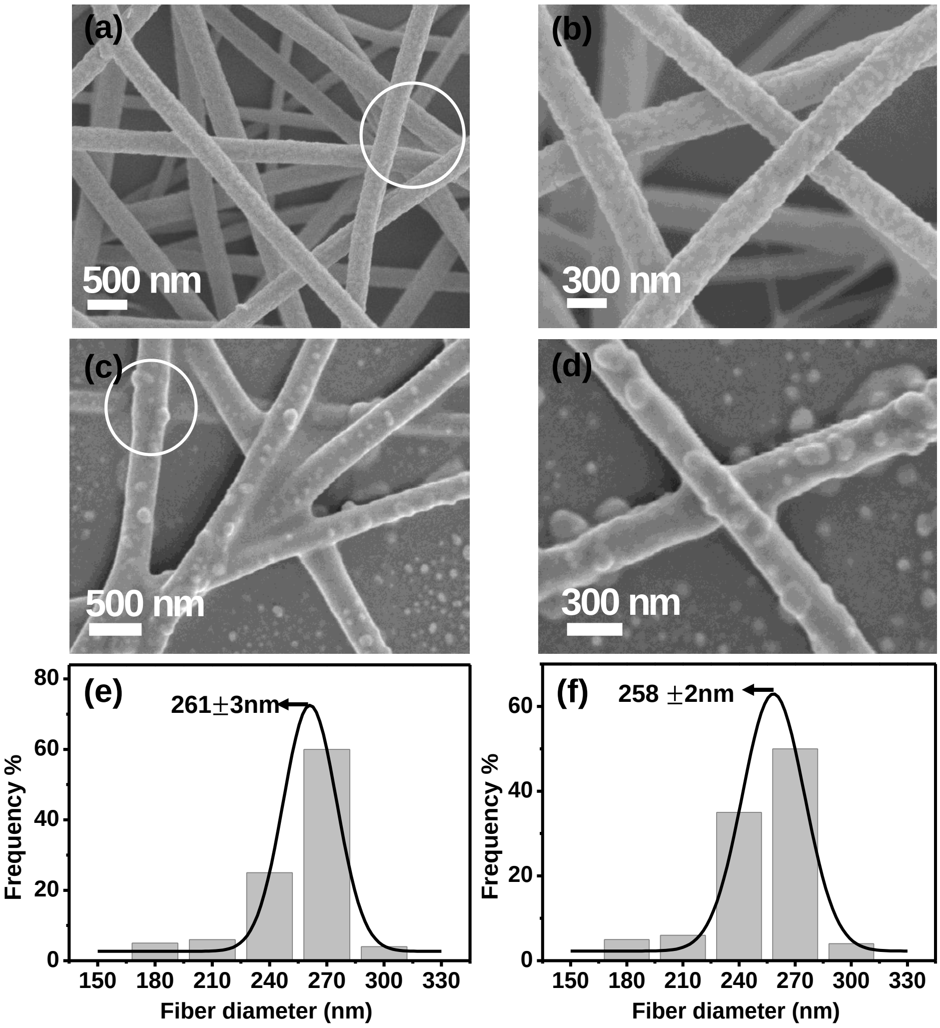

Fig. 3.5 SEM images of (a) and (b) is PVDF/$SnCl_2$ nanofiber and enlarged view of junction place, SEM images of (c) and (d) is Ag NFs and enlarged view of junction place (e) and (f) diameter distribution of PVDF/$SnCl_2$ nanofiber and Ag NFs.

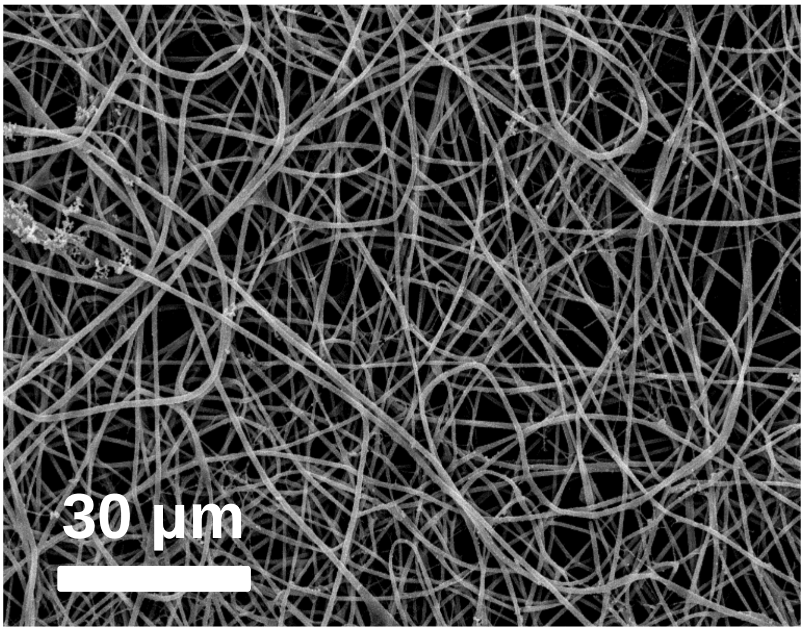

Fig. 3.6 Low resolution SEM image of PVDF/$SnCl_2$ nanofibers.

Fig. 3.7 shows the XRD patterns of synthesized Ag NFs by electroless deposition method. The observed diffraction peaks are well matched with JCPDS cards file No. 00-001-1164. The characteristic peaks of Ag are present at $2\theta = 38.16, 44.53, 64.72, 77.40$, and $82.06\,°$ due to the (111), (200), (220), (311), (222) lattice planes, respectively. The XRD results confirm the existing of Ag on the nanofibers.

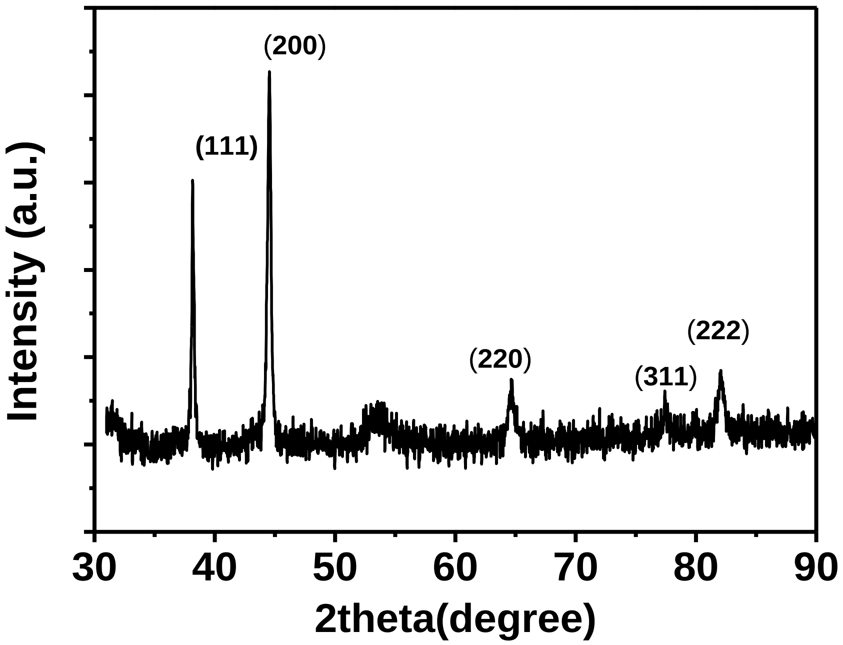

Fig. 3.7. XRD patterns of Ag NFs based film.

To further reveal the difference of the structure and composition of as-prepared nanofibers before and after electroless Ag deposition, high resolution morphology image, and their composition were observed by TEM and analyzed by EDS. Fig. 3.8 shows a typical TEM image of the PVDF/$SnCl_2$ nanofibers. The selected area electron diffraction (SAED) pattern is shown in Fig. 3.8 (c). These results reveal no crystal phase appearance. The corresponding EDS elemental map is necessary to confirm the composition of the nanofibers. The red color (Fig. 3.8 (e)) and green color (Fig. 3.8 (f)) in the EDS represent Sn and F characteristic radiation, respectively.

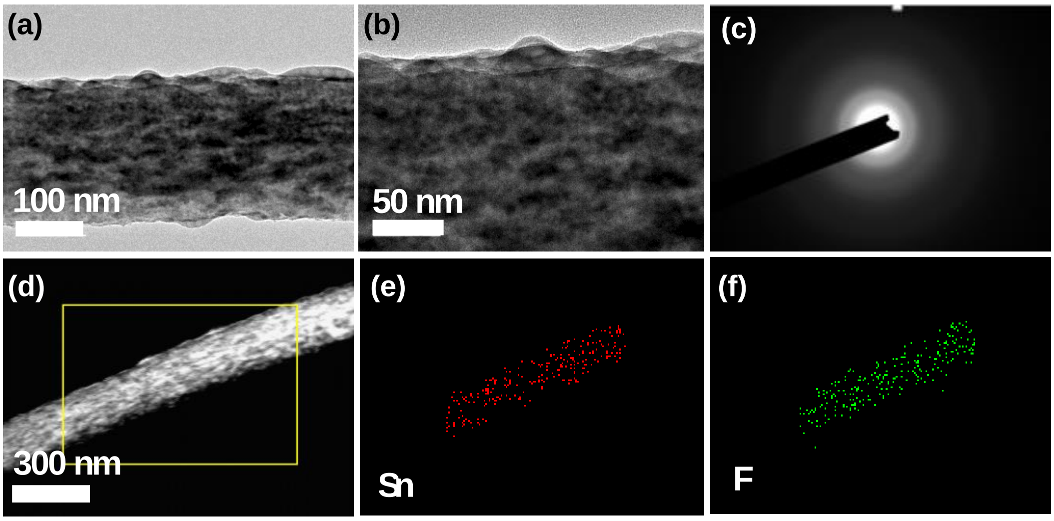

Fig. 3.8 (a) and (b) TEM image of PVDF/$SnCl_2$ nanofiber under different magnification. (c) SAED ring patterns of PVDF/$SnCl_2$ nanofiber, (d) the region for EDS mapping, (e) and (f) EDS mapping of Sn and F, respectively.

Fig. 3.9 (a) and (b) show the typical TEM image of Ag NFs. A great many particle thing appeared on the surface of the nanofiber. The inset of Fig. 3.9 (b) represent the distribution of the diameters of Ag nanoparticles (Ag NPs) attached on the nanofibers. The distribution ranges are approximately from 8 nm to 19 nm. The average diameter is approximately 10.68 nm. The Ag NPs are of uniform size and tightly packed together. Therefore, the small size and relatively uniform particles have coalesced with each other, mainly resulting in improved electrical conductivity[168]. The corresponding

SAED ring pattern is shown in Fig. 3.9 (c). The obtained Ag NPs on the nanofiber have face centered cubic (fcc) crystallographic structure. The four different diffraction planes corresponding to the (111), (200), (220), and (311), which reveals a fine crystallization in the Ag phase [169]. The high-resolution (HRTEM) image is shown in Fig.3.9 (d), revealing the lattice spacing of Ag nano-crystal is 0.21 nm that corresponds to the (200) plane of Ag.

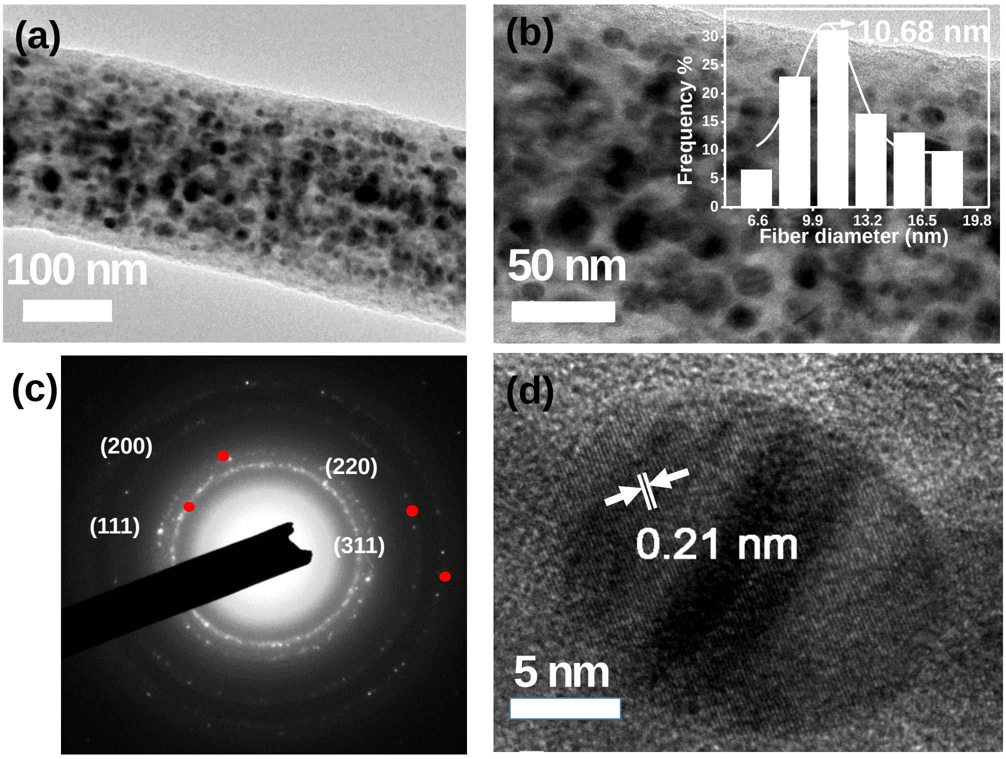

Fig. 3.9 (a) and (b) TEM image of Ag nanofiber under different magnification, inset of (b) distribution of the diameters of Ag NPs attached on the nanofibers. (c) SAED ring patterns of Ag NPs. (d) HRTEM image of Ag NPs.

The corresponding EDS elemental map of Ag NFs are shown in Fig. 3.10. The red color (Fig. 3.10 (b)) and green color (Fig. 3.10 (c)) in the EDS represent Ag and F characteristic radiation, respectively. Apparently, the results further confirm the existing of the component of Ag.

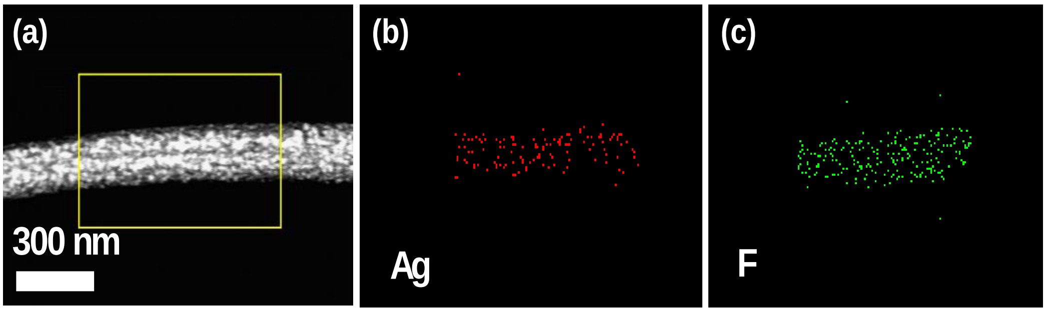

Fig. 3.10 (a) the region for Ag nanofiber EDS mapping, (b) and (c) EDS mapping of Ag and F, respectively.

3.3.4 Transmittance, Electrical, and Mechanical properties of Ag NFs.

Transmittance and sheet resistance are two important properties of transparent conductive film. Fig. 3.11 shows the wavelength dependent transmittance spectra of Ag NFs networks with the different thicknesses (sample 1 and 2 were prepared under different electrspinning duration, 1 min and 2 min, respectively. Therefore, nanofibers of the sample 2 is thicker than that of the sample 1). As shown in Fig. 3.11, the three solid line is regard to sample 1, they are original PVDF/$SnCl_2$ nanofiber, catalyst Ag seed attached on the nanofibers (after EAD first step), and lots of Ag particles deposited on the nanofiber (after EAD second step), respectively. Similarly, the three dotted line is according to the sample 2 under same conditions as the solid lines. As we can see, the transmittance decreases as the thickness increases. The average transmittances of the nanofibers of sample 1 are 97%， 95% (after first step of EAD), and 84% (accomplishing EAD), respectively, which were measured over wavelengths of 300-800 nm. The size of the empty areas between nanofibers is usually larger than the wavelength of light, which give chance to allow a broad band of light to transmit. Thus, the large empty areas between the nanofibers contribute the transmittance of electrospinning nanofibers. The decay of the transmittance of the three nanofibers under different conditions was caused by the attachment of Ag seeds and Ag particles. Ag seeds and particles may occupy some space of the empty area, so the transmittance of the nanofibers based thin film is decreased. The transmittance results for sample 2 also show the same decreased trends, which were from 91%, to 84%, and to 75% in the end.

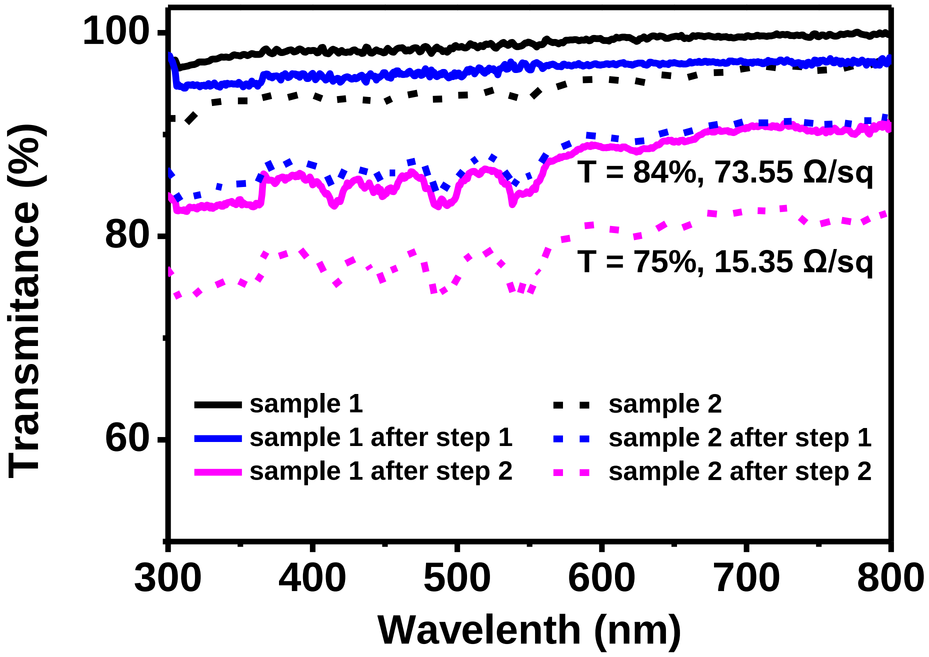

Fig. 3.11 Wavelength dependent transmittance spectra of Ag NFs networks with respect to the two group of nanofibers with different thickness, the solid lines are original PVDF/$SnCl_2$ nanofibers by electrspinning 1 min (Black), Ag seed attached on nanofibers (blue), and Ag particles distributed on the nanofibers (pink); Dotted line are original PVDF/$SnCl_2$ nanofibers by electrspinning 2 mins (Black), Ag seed attached on nanofibers (blue), and Ag particles distributed on the nanofibers (pink)

We have performed four-probe DC measurement for Ag nanofiber based film with different density and plotted their sheet resistance (*Rs*) as a function of electrspining time in Fig. 3.12. As can be seen from Fig. 3.12, the sheet resistance *Rs* of Ag NFs film is dramatically decreased from 73.55 Ω $\square^{-1}$ (T ~ 84%, electrspinning 1 min) to 0.46 Ω $\square^{-1}$ (T ~ 66%, electrospinning 7 min) with the increasing electrspinning duration time (increasing density). In general, the sheet resistance of the nanofibers based film is depended on two factors. One is the dimensions of the NFs themselves, the other one is the density of NWs (the number of NFs). First, each electrospinning NF is extremely long, covering the entire surface. [169] The sheet resistance of the network decreases along with the length of the increases. This theory is studied by G. GrUner *et al* [170]. The model of percolation theory is shown in following equation (3.1), which predicts that the *Nc* (critical density corresponding to the percolation threshold) dramatically decreases when the length *1D* nanomaterials increases. The longer NFs need fewer wires to form a conductive path across a given space, so that decreases the number of junctions and thus lower the resistance.

In our study, the dimensions of Ag NFs that were used to measure the sheet resistance have no great difference, therefore, the density of the NFs plays a crucial role in the conductivity. There already have great many studies, showing that the sheet resistance decreases with the increasing NFs density (increasing number of NFs)[154,171,172]. This result also follow the percolation theory proposed by G. GrUner et al, which predicts that the conductivity is dependency of the density as shown in equation (3.2)

where σ refers to the conductivity, *N* is the density of NFs. Therefore, the sheet resistance remarkable decreased as the density of NFs increases.

As for transparent conductive electrodes, balancing the properties optical and electrical properties usually especially important. Adjusting the two properties depends on different applications.

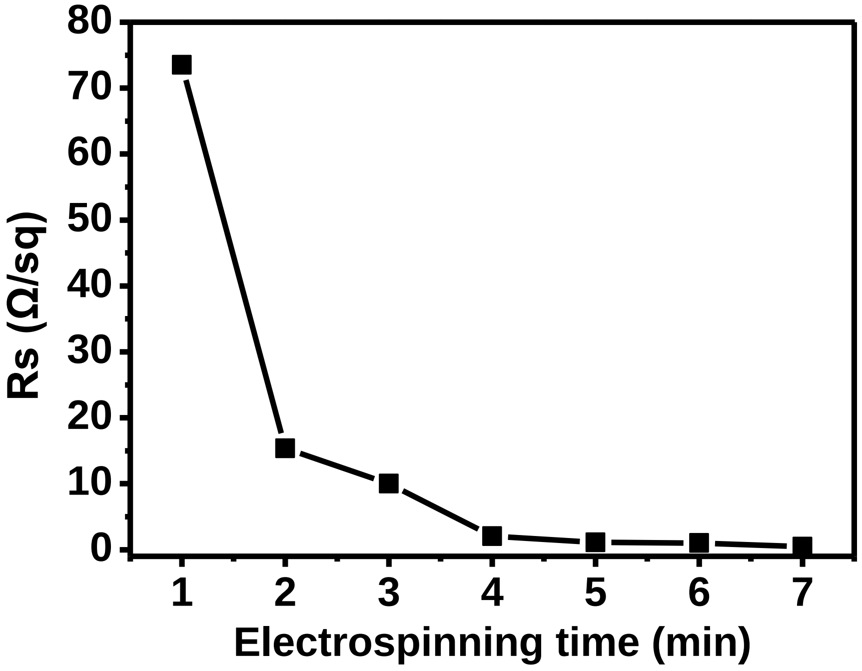

Fig. 3.12 Sheet resistance as a function of electrospining time of Ag nanofiber based conductive film.

Our Ag NFs electrodes are bendable and foldable. To examine the mechanical durability, the sample was bended down to the degree, showing like the inset of Fig. 3.13. Repetitively bent the film 100 times, and collect the value of *Rs* systematically, the result shows in Fig. 3.13. They are 1.9, 1.9, 1.92, 1.98, 2, 2.05, 2.25, 2.3, 2.32, 2.35, 2.4 Ω □$^{-1}$. No obvious degradation observed in electrical conductivity. Thus, the Ag NFs TCE possess excellent mechanical stability.

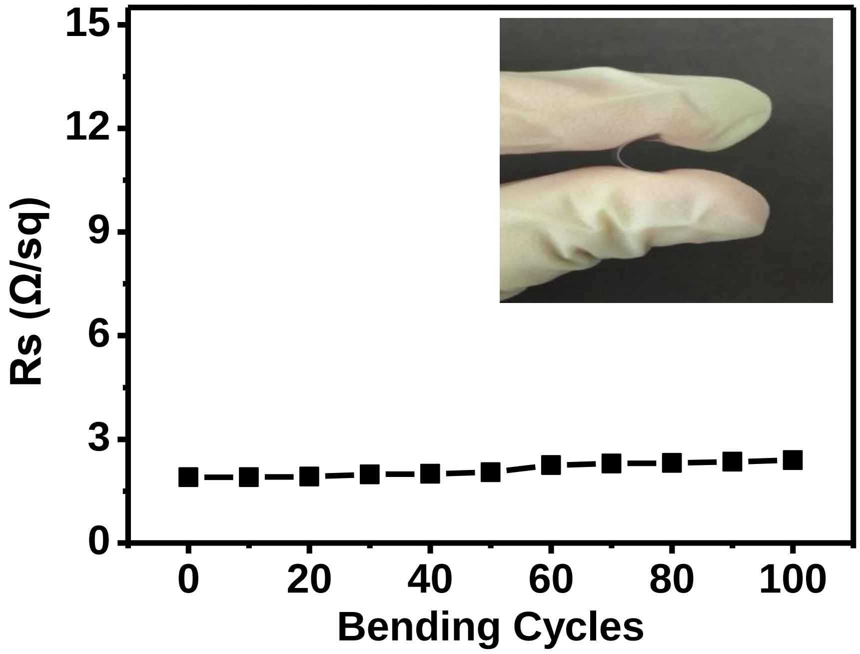

Fig. 3.13 Change in *Rs* after bending as a function of bending cycles for Ag NFs based film. The inset shows the bending degree of each bending process.

3.3.5 Rs-T for Ag NFs transparent electrode.

Fig. 3.14 shows the sheet resistance and transmittance (at λ= 550 nm) *(Rs – T)* relationships. We measured the optoelectronic performance of the Ag NFs with different thickness (with different electrospining duration). For this Ag NFs film produced by ELD, the optical transmittance at 550 nm is 84% with *Rs* around 75 Ω □$^{-1}$, which is close to the optoelectronic requirement for touch screen panels[173]. We further make a comparison for the performance of the Ag NFs with other alternative materials, including ITO [23], single wall carbon nanotube (SWCNT) [157], and poly(3,4-ethylenedioxythiophene):poly(styrenesulfonate) (PEDOT:PSS) [107], Graphene [117], solution-processed silver nanowires (Ag NWs) [174], metal grids (Ag grids) [175], thin Ni film [176]. According to the result shown in the Fig. 3.13. The conductivity performance of Ag NWs is higher than that of others. A commonly used figure of merit for transparent conducting electrode is the ratio of electrical conductance to optical conductance, which is for comparing the performance of a film by the equation as follows[177]:

where is the optical conductance (here collected at λ= 550 nm), is the electrical conductance of the film. This expression has been used to describe many transparent conductive films. The ratio () of this Ag NFs reached to 80 when *Rs* is 15.35 Ω □$^{-1}$ (T = 75%). This is much higher than other transparent electrodes, such as for graphene ~ 0.5, and for nanotubes ~ 25 [120].

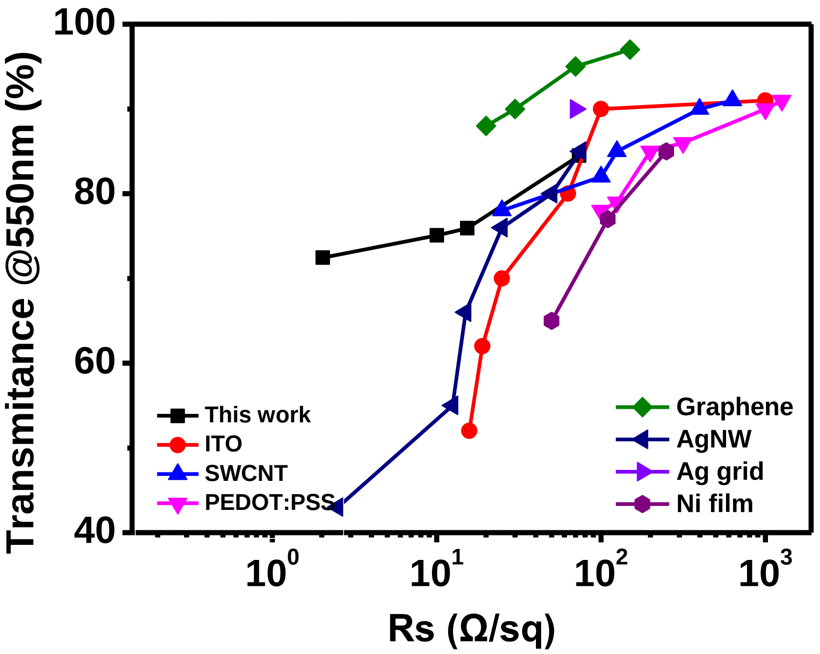

Fig. 3.14 Transmission (at 550 nm) and *Rs* values of AgNFs and comparison with typical transparent conductors, including ITO, SWCNT, PEDOT:PSS，Graphene, Ag NW, Ag grid, Ni film.

3.4 Summary

In summary, simplest method to prepare Ag nanofibers based transparent conductive electrode is presented. In particular, the synthesis of Ag NFs TCE possess high conductive properties, and the factors affecting electrospinning and reaction mechanism of Ag NPs are easily controlled. Significant advantages of this work include: the whole process has a short preparation and reaction time; relatively uniform precursor PVDF/$SnCl_2$ nanofibers were produced; uniform, small, and tightly connected Ag NPs were obtained and closely attached on the nanofibers and to form the Ag NFs; the whole fabrication process proceeds at room temperature; organic solvent are not used, and all raw material are cheap, and easy to deal with; no hazardous by-products and all step is environmentally friendly. Therefore, the easy process of electrospinning and electroless metallic deposition can contribute to saving energy and reduce the cost of preparing Ag NFs TCE. These advantages make the methods practically useful and potentially applicable to large-scale industrial manufacture of stage TCE, which shows great potential for widespread commercial use in a variety of applications.

Chapter 4

Conclusions and Future outlook

4.1 Conclusion

Considering this enormous portion of energy use, it is imperative to develop sustainable energy source. In this thesis, we successfully fabricated a rectification-free piezo-supercapacitor, which integrates both supercapacitor and piezoelectric energy harvesting layer into one hybridized device. The flexible piezoelectric PVDF film can convert mechanical vibration into a built-in electric-field, which serves as the driving force for the migration of ions towards the interface of the FCC electrodes. The asymmetric characteristics of the PVDF thin film during compress and relaxation stages results in the effective charging without any rectification device. The flexible piezo-supercapacitor exhibits that it can maintain high mechanical strength and high capacitance simultaneously under the bending and stretching test, and shows stable electrochemical performance with the energy density of 49.67 mWh/m^2 and the power density of 400 mW/m^2. Our device can be further extended for providing sustainable power source of various types of sensors.

On the other hand, we show a thin, flexible conducting Ag NFs transparent electrode with excellent conductivity of 73.55 Ω $\square^{-1}$ and 15.35 Ω $\square^{-1}$ (transmittance of 84% and 75%) by combining electrospinning of PVDF nanofiber and electroless deposition of Ag methods. The commonly used figure of merit for transparent conductors, the ratio of electric conductance to optical conductance () reached to 80 when *Rs* is 15.35 Ω $\square^{-1}$ (T = 75%). In addition, this Ag NFs transparent electrode is flexible and shown with good stability. The entire processes were accomplished at room temperature, which give rise to the possibility of large-scale and low-cost fabrication for electronic devices. This transparent Ag NFs electrode shows great potential for widespread commercial use in a variety of applications.

In summary, different synthesis techniques and novel concepts have been proposed and developed. PVDF with different morphologies have been utilized in our works. PVDF thin film worked as mechanical energy harvester and separator of supercapacitor. PVDF nanofiber was used as a template for preparing Ag nanowires.

4.2 Further work

As discussed in this thesis, the rectification-free piezo-supercapacitors have been designed and fabricated. The novel fundamental mechanism for directly converted and simultaneously stored mechanical energy as electrochemical energy is accomplished. Recently, a new aluminum-ion rechargeable battery system have been proposed, which offers the possibility of high specific capacity (~ 70 mAh/g), high energy density (~ 40 Wh/kg, comparable to lead-acid and Ni-MH batteries), high power density (~3000 W/kg, similar to supercapacitor), long cyclic life (more than 7,500 cycles without capacity decay), low cost, and low flammability[178]. Great strides have been made on such rechargeable Al-ion battery, and open up the possibility for new applications. However, studies according to Al-ion battery are still at their early stage, more applications and different types of Al-based electrode and electrolyte should be further developed. Therefore, in the future work, we propose to further construct a rectification-free system by combining piezo-nanogenerator with Al-ion battery to be a new electronic device.

On the other hand, Ag NFs based transparent conducting electrode with good transmittance, low sheet resistance, and robust mechanical stability have been fabricated. Our Ag NFs transparent electrode have chance to be a good candidate applied in solar cells. In addition, it is expected to further investigate the junction resistance between two nanofibers. Further explore the mechanism and systematically investigate the influence of single junction resistance to sheet resistance of transparent conducting electrodes.

Reference

1. Lovelock, J. *The Revenge of Gaia: Earth's Climate Change and the Crisis of Humanity*. (2006).

2. Aricò, A. S., Bruce, P., Scrosati, B., Tarascon, J.-M. & van Schalkwijk, W. Nanostructured materials for advanced energy conversion and storage devices. *Nat. Mater.* **4,** 366–377 (2005).

3. Baughman, R. H., Zakhidov, A. A. & de Heer, W. A. Carbon nanotubes--the route toward applications. *Science* **297,** 787–792 (2002).

4. Cabana, J., Monconduit, L., Larcher, D. & Palacín, M. R. Beyond intercalation-based Li-ion batteries: The state of the art and challenges of electrode materials reacting through conversion reactions. *Adv. Mater.* **22,** E170–E192 (2010).

5. Cai, X., Peng, M., Yu, X., Fu, Y. & Zou, D. Flexible planar/fiber-architectured supercapacitors for wearable energy storage. *J. Mater. Chem. C* **2,** 1184–1200 (2014).

6. Dai, L. Functionalization of graphene for efficient energy conversion and storage. *Acc. Chem. Res.* **46,** 31–42 (2013).

7. El-Kady, M. F. & Kaner, R. B. Scalable fabrication of high-power graphene micro-supercapacitors for flexible and on-chip energy storage. *Nat. Commun.* **4,** 1475–1484 (2013).

8. Guo, Y. G., Hu, J. S. & Wan, L. J. Nanostructured materials for electrochemical energy conversion and storage devices. *Adv. Mater.* **20,** 2878–2887 (2008).

9. Harries, D. N., Paskevicius, M., Sheppard, D. A., Price, T. E. C. & Buckley, C. E. Concentrating solar thermal heat storage using metal hydrides. in *Proceedings of the IEEE* **100,** 539–549 (2012).

10. Huang, X. L. *et al.* Homogeneous CoO on graphene for binder-free and ultralong-life lithium ion batteries. *Adv. Funct. Mater.* **23,** 4345–4353 (2013).

11. Sahoo, N. G., Pan, Y., Li, L. & Chan, S. H. Graphene-based materials for energy conversion. *Adv. Mater.* **24,** 4203–4210 (2012).

12. Wang, Y. *et al.* Silicon nanowires for biosensing, energy storage, and conversion. *Advanced Materials* **25,** 5177–5195 (2013).

13. Xu, C. *et al.* Graphene-based electrodes for electrochemical energy storage. *Energy Environ. Sci.* **6,** 1388 (2013).

14. Priya, S. & Inman, D. J. *Energy harvesting technologies*. *Energy Harvesting Technologies* (2009). doi:10.1007/978-0-387-76464-1

15. Hu, Y. & Wang, Z. L. Recent progress in piezoelectric nanogenerators as a sustainable power source in self-powered systems and active sensors. *Nano Energy* **14,** 3–14 (2015).

16. Swallow, L. M., Luo, J. K., Siores, E., Patel, I. & Dodds, D. A piezoelectric fibre composite based energy harvesting device for potential wearable applications. *Smart Mater. Struct.* **17,** 025017 (2008).

17. Xia, X.-H., Tu, J.-P., Wang, X.-L., Gu, C.-D. & Zhao, X.-B. Mesoporous Co3O4 monolayer hollow-sphere array as electrochemical pseudocapacitor material. *Chem. Commun. (Camb).* **47,** 5786–5788 (2011).

18. Xiang, F.-X., Wang, X.-L. & Dou, S.-X. Transport evidence for the coexistence of the topological surface state and a two-dimensional electron gas in BiSbTe3 topological insulator. *arXiv Prepr.* **1404,** 11 (2014).

19. Xu, B. *et al.* Activated carbon fiber cloths as electrodes for high performance electric double layer capacitors. *Electrochim. Acta* **52,** 4595–4598 (2007).

20. Yang, C. & Liu, P. Polypyrrole/conductive mica composites: Preparation, characterization, and application in supercapacitor. *Synth. Met.* **160,** 768–773 (2010).

21. Zhang, K., Zhang, L. L., Zhao, X. S. & Wu, J. Graphene/polyaniline nanofiber composites as supercapacitor electrodes. *Chem. Mater.* **22,** 1392–1401 (2010).

22. Zhang, L. L. & Zhao, X. S. Carbon-based materials as supercapacitor electrodes. *Chem. Soc. Rev.* **38,** 2520–2531 (2009).

23. Hecht, D. S., Hu, L. & Irvin, G. Emerging transparent electrodes based on thin films of carbon nanotubes, graphene, and metallic nanostructures. *Adv. Mater.* **23,** 1482–1513 (2011).

24. Bailato, A. Piezoelectricity: History and New Thrusts. *IEEE* **1,** 575–583 (1996).

25. On the Piezoelectric Effect of Bone. *J. Phys. socity Japan* **12,** 1158–1162 (1957).

26. Ter-Gazarian, A. *Energy Storage for Power Systems*. (1994). doi:10.1049/PBPO063E

27. Temperature, U. *Usage Temperatures of Piezoceramic Materials Piezo Technologie*. **33,** (2013).

28. Anton, S. R. & Sodano, H. A. A review of power harvesting using piezoelectric materials (2003–2006). *Smart Materials and Structures* **16,** R1–R21 (2007).

29. Bowen, C. R., Kim, H. a., Weaver, P. M. & Dunn, S. Piezoelectric and ferroelectric materials and structures for energy harvesting applications. *Energy Environ. Sci.* **7,** 25–44 (2014).

30. Wen, X., Yang, W., Jing, Q. & Wang, Z. L. Harvesting broadband kinetic impact energy from mechanical triggering/vibration and water waves. *ACS Nano* **8,** 7405–7412 (2014).

31. Qin, Y., Wang, X. & Wang, Z. L. Microfibre-nanowire hybrid structure for energy scavenging. *Nature* **451,** 809–813 (2008).

32. Wang, Z. *et al.* (K,Na)NbO 3 Nanofiber-based Self-Powered Sensors for Accurate Detection of Dynamic Strain. *ACS Appl. Mater. Interfaces* **7,** 4921–4927 (2015).

33. Lee, J.-H. *et al.* Highly Sensitive Stretchable Transparent Piezoelectric Nanogenerator. *Energy Environ. Sci.* **6,** 169–175 (2013).

34. Gheibi, A., Latifi, M., Merati, A. A. & Bagherzadeh, R. Piezoelectric electrospun nanofibrous materials for self-powering wearable electronic textiles applications. *J. Polym. Res.* **21,** 1–7 (2014).

35. Beeby, S., Tudor, M. & White, N. Energy harvesting vibration sources for microsystems applications. (2006). doi:10.1088/0957-0233/17/12/R01

36. Saravanakumar, B., Soyoon, S. & Kim, S. Self-Powered pH Sensor Based on a Flexible Organic − Inorganic Hybrid Composite Nanogenerator. *ACS Appl. Mater. Interfaces* **6,** 13716–13723 (2014).

37. Bae, S., Kahya, O., Sharma, B. K., Kwon, J. & Cho, H. J. Graphene-P(VDF-TrFE) Multilayer Film for Flexible Applications - ACS Nano (ACS Publications). *ACS Nano* **4,** 3130–3138 (2013).

38. Chang, C., Tran, V. H., Wang, J., Fuh, Y. K. & Lin, L. Direct-write piezoelectric polymeric nanogenerator with high energy conversion efficiency. *Nano Lett.* **10,** 726–731 (2010).

39. Hinchet, R. *et al.* Performance optimization of vertical nanowire-based piezoelectric nanogenerators. *Adv. Funct. Mater.* **24,** 971–977 (2014).

40. Ottman, G. K., Hofmann, H. F., Bhatt, A. C. & Lesieutre, G. A. Adaptive piezoelectric energy harvesting circuit for wireless remote power supply. *IEEE Trans. Power Electron.* **17,** 669–676 (2002).

41. Whiter, R. a., Narayan, V. & Kar-Narayan, S. A Scalable Nanogenerator Based on Self-Poled Piezoelectric Polymer Nanowires with High Energy Conversion Efficiency. *Adv. Energy Mater.* **4,** n/a–n/a (2014).

42. Giannetti, E. Featured Article Semi-crystalline fluorinated polymers. *Polym. Int.* **50,** 10–26 (2001).

43. Li, L., Zhang, M., Rong, M. & Ruan, W. Studies on the transformation process of PVDF from α to β phase by stretching. *RSC Adv.* **4,** 3938 (2014).

44. Li, L., Zhang, M., Rong, M. & Ruan, W. Studies on the transformation process of PVDF from α to β phase by stretching. *RSC Adv.* **4,** 3938–3943 (2014).

45. Meyer, R. P. & Irvine, J. M. Identification by analysis of physiometric variation. (2006).

46. Choi, B. M. *et al.* Mechanically Powered Transparent Flexible Charge-Generating Nanodevices with Piezoelectric ZnO Nanorods. *Adv. Mater.* **21,** 2185–2189 (2009).

47. Hu, Y. *et al.* Self-Powered System with Wireless Data Transmission. *Nano Lett.* **11,** 2572–2577 (2011).

48. Liu, C., Li, F., Ma, L.-P. & Cheng, H.-M. Advanced materials for energy storage. *Adv. Mater.* **22,** E28–E62 (2010).

49. Dunn, B., Kamath, H. & Tarascon, J.-M. Electrical Energy Storage for the Grid: A Battery of Choices. *Science (80-.).* **334,** 928–935 (2011).

50. Miller. A brief history of supercapacitors. *Battey energy Technol.* **ISSN521452,** 61–78 (2007).

51. B.E.Conway. *Electrochemical supercapacitors*. (1999).

52. Faraji, S. & Nasir, F. The development supercapacitor from activated carbon by electroless plating — A review. *Renew. Sustain. Energy Rev.* **42,** 823–834 (2015).

53. Conway, B. E. Electrochemical science and technology. Transiton from 'Supercapacitor' to 'Battery' behavior in electrochemical energy storage. *J. Electrochem. Soc.* **138,** 1539–1548 (1991).

54. Zhang, L. L., Zhou, R. & Zhao, X. S. Graphene-based materials as supercapacitor electrodes. *J. Mater. Chem.* **20,** 5983 (2010).

55. Wei, W., Cui, X., Chen, W. & Ivey, D. G. Manganese oxide-based materials as electrochemical supercapacitor electrodes. *Chem. Soc. Rev.* **40,** 1697–1721 (2011).

56. Wang, Y. *et al.* Supercapacitor Devices Based on Graphene Materials. *J. Phys. Chem. C* **113,** 13103–13107 (2009).

57. Wang, Q., Wen, Z. & Li, J. A hybrid supercapacitor fabricated with a carbon nanotube cathode and a TiO2-B nanowire anode. *Adv. Funct. Mater.* **16,** 2141–2146 (2006).

58. Snook, G. a., Kao, P. & Best, A. S. Conducting-polymer-based supercapacitor devices and electrodes. *J. Power Sources* **196,** 1–12 (2011).

59. Frackowiak, E. Carbon materials for supercapacitor application. *Phys. Chem. Chem. Phys.* **9,** 1774–1785 (2007).

60. Abbey, C. & Joos, G. Supercapacitor energy storage for wind energy applications. *IEEE Trans. Ind. Appl.* **43,** 769–776 (2007).

61. Inagaki, M., Konno, H. & Tanaike, O. Carbon materials for electrochemical capacitors. *J. Power Sources* **195,** 7880–7903 (2010).

62. Wu, X.-L. & Xu, A.-W. Carbonaceous hydrogels and aerogels for supercapacitors. *J. Mater. Chem. A* **2,** 4852 (2014).

63. Bleda-Mart ńez, M. J. *et al.* Role of surface chemistry on electric double layer capacitance of carbon materials. *Carbon N. Y.* **43,** 2677–2684 (2005).

64. Futaba, D. N. *et al.* Shape-engineerable and highly densely packed single-walled carbon nanotubes and their application as super-capacitor electrodes. *Nat. Mater.* **5,** 987–994 (2006).

65. Guo, J. & Lua, A. C. Preparation of activated carbons from oil-palm-stone chars by microwave-induced carbon dioxide activation. *Carbon N. Y.* **38,** 1985–1993 (2000).

66. Hughes, M., Chen, G. Z., Shaffer, M. S. P., Fray, D. J. & Windle, a H. Electrochemical capacitance of a nanoporous composite of carbon nanotubes and polypyrrole. *Chem. Mater.* **14,** 1610–1613 (2002).

67. Hulicova, D., Yamashita, J., Soneda, Y., Hatori, H. & Kodama, M. Supercapacitors prepared from melamine-based carbon. *Chem. Mater.* **17,** 1241–1247 (2005).

68. Kierzek, K., Frackowiak, E., Lota, G., Gryglewicz, G. & Machnikowski, J. Electrochemical capacitors based on highly porous carbons prepared by KOH activation. *Electrochim. Acta* **49,** 515–523 (2004).

69. Augustyn, V., Simon, P. & Dunn, B. Pseudocapacitive oxide materials for high-rate electrochemical energy storage. *Energy Environ. Sci.* **7,** 1597 (2014).

70. Xia, X., Tu, J., Wang, X., Gu, C. & Zhao, X. Hierarchically porous NiO film grown by chemical bath deposition via a colloidal crystal template as an electrochemical pseudocapacitor material. *J. Mater. Chem.* **21,** 671 (2011).

71. Wang, D., Li, Y., Wang, Q. & Wang, T. Nanostructured Fe2O3–graphene composite as a novel electrode material for supercapacitors. *J. Solid State Electrochem.* **16,** 2095–2102 (2012).

72. Toupin, M., Brousse, T., Blanger, D. & Be, D. Charge Storage Mechanism of MnO Electrode Used in Aqueous Electrochemical Capacitor Charge Storage Mechanism of MnO 2 Electrode Used in Aqueous Electrochemical Capacitor. *Chem. Mater.* **16,** 3184–3190 (2004).

73. Subramanian, V., Zhu, H., Vajtai, R., Ajayan, P. M. & Wei, B. Hydrothermal synthesis and pseudocapacitance properties of MnO2 nanostructures. *J. Phys. Chem. B* **109,** 20207–20214 (2005).

74. Liu, J. *et al.* Co3O4 nanowire@MnO2 ultrathin nanosheet core/shell arrays: A new class of high-performance pseudocapacitive materials. *Adv. Mater.* **23,** 2076–2081 (2011).

75. Hu, C., Chang, K., Lin, M. & Wu, Y. Design and tailoring of the nanotubular arrayed architecture of hydrous RuO2 for next generation supercapacitors. *Nano Lett.* **6,** 2690–2695 (2006).

76. Ting, Y.-J. B., Wu, H., Kherani, N. P. & Lian, K. Development of pseudocapacitive molybdenum oxide–nitride for electrochemical capacitors. *Mater. Chem. Phys.* **154,** 118–124 (2015).

77. Pande, P. *et al.* Pseudocapacitive charge storage via hydrogen insertion for molybdenum nitrides. *J. Power Sources* **289,** 154–159 (2015).

78. Hwang, S. W. & Hyun, S. H. Synthesis and characterization of tin oxide/carbon aerogel composite electrodes for electrochemical supercapacitors. *J. Power Sources* **172,** 451–459 (2007).

79. Chen, C., Zhao, D., Xu, D. & Wang, X. γ-Mo2N/Co3Mo3N composite material for electrochemical supercapacitor electrode. *Mater. Chem. Phys.* **95,** 84–88 (2006).

80. Lu, Q., Chen, J. G. & Xiao, J. Q. Nanostructured electrodes for high-performance pseudocapacitors. *Angew. Chemie - Int. Ed.* **52,** 1882–1889 (2013).

81. Sivakkumar, S. R., Ko, J. M., Kim, D. Y., Kim, B. C. & Wallace, G. G. Performance evaluation of CNT/polypyrrole/MnO2 composite electrodes for electrochemical capacitors. *Electrochim. Acta* **52,** 7377–7385 (2007).

82. Ryu, K. S. *et al.* Poly(ethylenedioxythiophene) (PEDOT) as polymer electrode in redox supercapacitor. *Electrochim. Acta* **50,** 843–847 (2004).

83. Park, J. H., Ko, J. M., Park, O. O. & Kim, D.-W. Capacitance properties of graphite/polypyrrole composite electrode prepared by chemical polymerization of pyrrole on graphite fiber. *J. Power Sources* **105,** 20–25 (2002).

84. Hu, C. C. & Chu, C. H. Electrochemical impedance characterization of polyaniline-coated graphite electrodes for electrochemical capacitors - Effects of film coverage/thickness and anions. *J. Electroanal. Chem.* **503,** 105–116 (2001).

85. Chen, L. *et al.* Synthesis and pseudocapacitive studies of composite films of polyaniline and manganese oxide nanoparticles. *J. Power Sources* **195,** 3742–3747 (2010).

86. Kötz, R. & Carlen, M. Principles and applications of electrochemical capacitors. *Electrochim. Acta* **45,** 2483–2498 (2000).

87. Wang, G., Zhang, L. & Zhang, J. A review of electrode materials for electrochemical supercapacitors. *Chem. Soc. Rev.* **41,** 797 (2012).

88. Wang, K., Wu, H., Meng, Y. & Wei, Z. Conducting polymer nanowire arrays for high performance supercapacitors. *Small* **10,** 14–31 (2014).

89. Wang, K., Huang, J. & Wei, Z. Conducting Polyaniline Nanowire Arrays for High Performance Supercapacitors. *J. Phys. Chem. C* **114,** 8062–8067 (2010).

90. Zhang, D. *et al.* Transparent, Conductive, and Flexible Carbon Nanotube Films and Their Application in Organic Light-Emitting Diodes. *Nano Lett.* **6,** 1880–1886 (2006).

91. Wang, X., Zhi, L. & Mullen, K. Transparent, Conductive Graphene Electrodes for Solar Cells. *Nano Lett.* **8,** 323–327 (2007).

92. Granqvist, C. G. Transparent conductive electrodes for electrochromic devices: A review. *Appl. Phys. A Solids Surfaces* **57,** 19–24 (1993).

93. Conibeer, G. *et al.* Silicon nanostructures for third generation photovoltaic solar cells. *Thin Solid Films* **511-512,** 654–662 (2006).

94. Musa, a. ., Akomolafe, T. & Carter, M. . Production of cuprous oxide, a solar cell material, by thermal oxidation and a study of its physical and electrical properties. *Sol. Energy Mater. Sol. Cells* **51,** 305–316 (1998).

95. Wu, J. *et al.* Organic solar cells with solution-processed graphene transparent electrodes. *Appl. Phys. Lett.* **92,** 263302. (2008).

96. Van De Lagemaat, J. *et al.* Organic solar cells with carbon nanotubes replacing In2 O3: Sn as the transparent electrode. *Appl. Phys. Lett.* **88,** 10–13 (2006).

97. Rowell, M. W. *et al.* Organic solar cells with carbon nanotube network electrodes. *Appl. Phys. Lett.* **88,** 86–89 (2006).

98. Kay, A. & Grätzel, M. Low cost photovoltaic modules based on dye sensitized nanocrystalline titanium dioxide and carbon powder. *Sol. Energy Mater. Sol. Cells* **44,** 99–117 (1996).

99. Pang, S., Hernandez, Y., Feng, X. & Müllen, K. Graphene as transparent electrode material for organic electronics. *Adv. Mater.* **23,** 2779–2795 (2011).

100. Krebs, F. C. Fabrication and processing of polymer solar cells: A review of printing and coating techniques. *Sol. Energy Mater. Sol. Cells* **93,** 394–412 (2009).

101. Li, G., Chu, C. W., Shrotriya, V., Huang, J. & Yang, Y. Efficient inverted polymer solar cells. *Appl. Phys. Lett.* **88,** 23–25 (2006).

102. Headley, S. A new day dawning. *Youth Stud. Aust.* **32,** 1–2 (2013).

103. Wolf, M. Limitations and Possibilities for Improvement of Photovoltaic Solar Energy Converters: Part I: Considerations for Earth's Surface Operation. *Proc. IRE* **48,** 583–595 (1960).

104. Wang, X. *et al.* Transparent carbon films as electrodes in organic solar cells. *Angew. Chemie - Int. Ed.* **47,** 2990–2992 (2008).

105. Kang, M. G., Kim, M. S., Kim, J. S. & Guo, L. J. Organic Solar Cells Using Nanoimprinted Transparent Metal Electrodes. *Adv. Mater.* **20,** 4408–4413 (2008).

106. Zou, J., Yip, H. L., Hau, S. K. & Jen, A. K. Y. Metal grid/conducting polymer hybrid transparent electrode for inverted polymer solar cells. *Appl. Phys. Lett.* **96,** 203301 (2010).

107. Pasquier, A. Du, Unalan, H. E., Kanwal, A., Miller, S. & Chhowalla, M. Conducting and transparent single-wall carbon nanotube electrodes for polymer-fullerene solar cells. *Appl. Phys. Lett.* **87,** 1–3 (2005).

108. O'Regan, B. & Grätzel, M. A low-cost, high-efficiency solar cell based on dye-sensitized colloidal TiO2 films. *Nature* **353,** 737–740 (1991).

109. Kumar, A. & Zhou, C. The race to replace tin-doped indium oxide: Which material will win? *ACS Nano* **4,** 11–14 (2010).

110. Hong, W., Xu, Y., Lu, G., Li, C. & Shi, G. Transparent graphene/PEDOT-PSS composite films as counter electrodes of dye-sensitized solar cells. *Electrochem. commun.* **10,** 1555–1558 (2008).

111. Kim, Y. H. *et al.* Highly conductive PEDOT:PSS electrode with optimized solvent and thermal post-treatment for ITO-free organic solar cells. *Adv. Funct. Mater.* **21,** 1076–1081 (2011).

112. Vosgueritchian, M., Lipomi, D. J. & Bao, Z. Highly conductive and transparent PEDOT:PSS films with a fluorosurfactant for stretchable and flexible transparent electrodes. *Adv. Funct. Mater.* **22,** 421–428 (2012).

113. Ouyang, J. 'secondary doping' methods to significantly enhance the conductivity of PEDOT:PSS for its application as transparent electrode of optoelectronic devices. *Displays* **34,** 423–436 (2013).

114. Wu, Z. *et al.* Transparent, Conductive Carbon Nanotube Films. *Science (80-.).* **305,** 1273–1276 (2004).

115. Zhang, M., Fang, S., Zakhidov, A. A., Lee, S. B. & Baughman, R. H. Strong, Transparent, Multifunctional, Carbon Nanotube Sheets. *Science (80-.).* **309,** 1215–1220 (2005).

116. Li, X. *et al.* Transfer of large-area graphene films for high-performance transparent conductive electrodes. *Nano Lett.* **9,** 4359–4363 (2009).

117. Bae, S. *et al.* Roll-to-roll production of 30-inch graphene films for transparent electrodes. *Nat. Nanotechnol.* **5,** 574–578 (2010).

118. Kim, K. S. *et al.* Large-scale pattern growth of graphene films for stretchable transparent electrodes. *Nature* **457,** 706–710 (2009).

119. Gaynor, W., Burkhard, G. F., McGehee, M. D. & Peumans, P. Smooth nanowire/polymer composite transparent electrodes. *Adv. Mater.* **23,** 2905–2910 (2011).

120. De, S. *et al.* Silver Nanowire Networks as Flexible ,. *ACSNano* **3,** 1767–1774 (2009).

121. Hsu, P.-C. *et al.* Performance enhancement of metal nanowire transparent conducting electrodes by mesoscale metal wires. *Nat. Commun.* **4,** 2522 (2013).

122. Coskun, S., Selen Ates, E. & Unalan, H. E. Optimization of silver nanowire networks for polymer light emitting diode electrodes. *Nanotechnology* **24,** 125202 (2013).

123. Hsu, P. C. *et al.* Electrolessly deposited electrospun metal nanowire transparent electrodes. *J. Am. Chem. Soc.* **136,** 10593–10596 (2014).

124. Lee, S. M., Lee, J. H. & Bak, S. Hybrid windshield-glass heater for commercial vehicles fabricated via enhanced electrostatic interactions among a substrate, silver nanowires, and an over-coating layer. *Nano Res.* 1–11 (1998).

125. Zeng, X. Y., Zhang, Q. K., Yu, R. M. & Lu, C. Z. A new transparent conductor: Silver nanowire film buried at the surface of a transparent polymer. *Adv. Mater.* **22,** 4484–4488 (2010).

126. Wu, H. *et al.* A transparent electrode based on a metal nanotrough network. *Nat. Nanotechnol.* **8,** 421–5 (2013).

127. Huskinson, B. *et al.* A metal-free organic-inorganic aqueous flow battery. *Nature* **505,** 195–198 (2014).

128. Zou, Z., Ye, J., Sayama, K. & Arakawa, H. Direct splitting of water under visible light irradiation with an oxide semiconductor photocatalyst. *Nature* **414,** 625–627 (2001).

129. Gutfleisch, O. *et al.* Magnetic materials and devices for the 21st century: Stronger, lighter, and more energy efficient. *Advanced Materials* **23,** 821–842 (2011).

130. Tu, W., Zhou, Y. & Zou, Z. Photocatalytic conversion of CO2 into renewable hydrocarbon fuels: State-of-the-art accomplishment, challenges, and prospects. *Advanced Materials* **26,** 4607–4626 (2014).

131. Karabelli, D., Leprêtre, J. C., Alloin, F. & Sanchez, J. Y. Poly(vinylidene fluoride)-based macroporous separators for supercapacitors. *Electrochim. Acta* **57,** 98–103 (2011).

132. Hwang, K., Kwon, B. & Byun, H. Preparation of PVdF nanofiber membranes by electrospinning and their use as secondary battery separators. *J. Memb. Sci.* **378,** 111–116 (2011).

133. Sodano, H. a. Comparison of Piezoelectric Energy Harvesting Devices for Recharging Batteries. *J. Intell. Mater. Syst. Struct.* **16,** 799–807 (2005).

134. Park, T., Kim, B., Kim, Y. & Kim, E. Highly conductive PEDOT electrodes for harvesting dynamic energy through piezoelectric conversion. *J. Mater. Chem. A* **2,** 5462–5469 (2014).

135. Xie, Y. *et al.* Stretchable all-solid-state supercapacitor with wavy shaped polyaniline/graphene electrode. *J. Mater. Chem. A* **2,** 9142–9149 (2014).

136. Li, Z., Zhang, X. & Li, G. In situ ZnO nanowire growth to promote the PVDF piezo phase and the ZnO-PVDF hybrid self-rectified nanogenerator as a touch sensor. *Phys. Chem. Chem. Phys.* **16,** 5475–5479 (2014).

137. Hu, Y. & Wang, Z. L. Recent progress in piezoelectric nanogenerators as a sustainable power source in self-powered systems and active sensors. *Nano Energy* (2015). doi:10.1016/j.nanoen.2014.11.038

138. Park, K. Il *et al.* Highly-efficient, flexible piezoelectric PZT thin film nanogenerator on plastic substrates. *Adv. Mater.* **26,** 2514–2520 (2014).

139. Pradel, K. C., Wu, W., Ding, Y. & Wang, Z. L. Solution-Derived ZnO Homojunction Nanowire Films on Wearable Substrates for Energy

Conversion and Self-Powered Gesture Recognition. *Nano Lett.* **14,** 6897–6905 (2014).

140. Ramadoss, A. *et al.* Piezoelectric-Driven Self-Charging Supercapacitor Power Cell. *ACS Nano* **9,** 4337–4345 (2015).

141. Wang, C. H. *et al.* Optimization of the output efficiency of GaN nanowire piezoelectric nanogenerators by tuning the free carrier concentration. *Adv. Energy Mater.* **4,** 1400392– 1400399 (2014).

142. Xue, X. *et al.* Surface free-carrier screening effect on the output of a ZnO nanowire nanogenerator and its potential as a self-powered active gas sensor. *Nanotechnology* **24,** 225501–225507 (2013).

143. Yu, R., Pan, C., Chen, J., Zhu, G. & Wang, Z. L. Enhanced performance of a ZnO nanowire-based self-powered glucose sensor by piezotronic effect. *Adv. Funct. Mater.* **23,** 5868–5874 (2013).

144. Zhong, J. *et al.* Fiber-based generator for wearable electronics and mobile medication. *ACS Nano* **8,** 6273–6280 (2014).

145. Xing, L., Nie, Y., Xue, X. & Zhang, Y. PVDF mesoporous nanostructures as the piezo-separator for a self-charging power cell. *Nano Energy* **10,** 44–52 (2014).

146. Xue, X. *et al.* Flexible self-charging power cell for one-step energy conversion and storage. *Adv. Energy Mater.* **4,** 1301329–1301334. (2014).

147. Xue, X., Wang, S., Guo, W., Zhang, Y. & Wang, Z. L. Hybridizing energy conversion and storage in a mechanical-to- electrochemical process for self-charging power cell. *Nano Lett.* **12,** 5048–5054 (2012).

148. Hu, L. *et al.* Stretchable, porous, and conductive energy textiles. *Nano Lett.* **10,** 708–714 (2010).

149. Tang, W. M., Jin, H. Y., Peng, Z. H. & Chan, H. Controllable functionalized carbon fabric for high-performance all-carbon-based supercapacitors. *RSC Adv.* **4,** 33022–33028 (2014).

150. Zhang, L. L. & Zhao, X. S. Carbon-based materials as supercapacitor electrodes. *Chem. Soc. Rev.* **38,** 2520–2531 (2009).

151. Zhu, Y. *et al.* Carbon-based supercapacitors produced by activation of graphene. *Science* **332,** 1537–1541 (2011).

152. Zhu, R. *et al.* Fused silver nanowires with metal oxide nanoparticles and organic polymers for highly transparent conductors. *ACS Nano* **5,** 9877–9882 (2011).

153. Spinelli, P. & Polman, A. Transparent Conducting Silver Nanowire Networks. *ACS Nano* **12,** 3138–3144 (2012).

154. Langley, D. *et al.* Flexible transparent conductive materials based on silver nanowire networks: a review. *Nanotechnology* **24,** 452001 (2013).

155. Akter, T. & Kim, W. S. Reversibly Stretchable Transparent Conductive Coatings of Spray- Deposited Silver Nanowires(supporting). *ACS Appl. Mater. Interfaces* 1–3 (2012). doi:10.1021/am300058j

156. Hu, L., Wu, H. & Cui, Y. Metal nanogrids, nanowires, and nanofibers for transparent electrodes. *MRS Bull.* **36,** 760–765 (2011).

157. Barnes, T. M. *et al.* Single-wall carbon nanotube networks as a transparent back contact in CdTe solar cells. *Appl. Phys. Lett.* **90,** 24–26 (2007).

158. Tadros, M. E., Mason, J. A. & Kadoch, C. A. Oxide coated metal grid electrode structure in displays devices. U.S. Patent 5,293,546[P] (1994).

159. Lee, J. *et al.* Very long Ag nanowire synthesis and its application in a highly transparent, conductive and flexible metal electrode touch panel. *Nanoscale* **4,** 6408 (2012).

160. Lee, H. *et al.* Highly bendable, conductive, and transparent film by an enhanced adhesion of silver nanowires. *ACS Appl. Mater. Interfaces* **5,** 9155–9160 (2013).

161. Guo, C., Zhou, L. & Lv, J. Effects of expandable graphite and modified ammonium polyphosphate on the flame-retardant and mechanical properties

of wood flour-polypropylene composites. *Polym. Polym. Compos.* **21,** 449–456 (2013).

162. Song, Tze-Bin, Yu Chen, Choong-Heui Chung, Yang Yang, Brion Bob, Hsin-Sheng Duan, Gang Li, King-Ning Tu, Yu Huang, and Y. Y. Nanoscale Joule heating and electromigraton enhanced ripening of silver nanowire contacts Nanoscale Joule heating and electromigraton enhanced ripening of silver nanowire contacts. *ACS Nano* **8,** 2804–2811 (2014).

163. Nanowire, S. *et al.* Scalable Coating and Properties of transparent Ag nanowire. *ACS Nano* **4,** 2955–2963 (2010).

164. Zhang, L. *et al.* Kinetically controlled synthesis of large-scale morphology-tailored silver nanostructures at low temperature. *Nanoscale* **7,** 13420–13426 (2015).

165. Tao, G., Gong, a., Lu, J., Sue, H. J. & Bergbreiter, D. E. Surface functionalized polypropylene: Synthesis, characterization, and adhesion properties. *Macromolecules* **34,** 7672–7679 (2001).

166. Lin, J., Wang, W. & Chou, S. Flexible carbon nanotube / polypropylene composite plate decorated with poly (3 , 4-ethylenedioxythiophene) as ef fi cient counter electrodes for dye-sensitized solar cells. *J. Power Sources* **282,** 348–357 (2015).

167. Lee, C.-L. & Syu, C.-C. Ag nanoparticle as a new activator for catalyzing electroless copper bath with 2,2′-bipyridyl. *Electrochim. Acta* **56,** 8880–8883 (2011).

168. Yang, Y., Jia, Z., Li, Q. & Guan, Z. Experimental investigation of the governing parameters in the electrospinning of polyethylene oxide solution. *IEEE Trans. Dielectr. Electr. Insul.* **13,** 580–584 (2006).

169. Dong, X., Wang, J., Cui, Q., Liu, G. & Yu, W. Preparation of LaFeO3 Porous Hollow Nanofibers by Electrospinning. *Int. J. Chem.* **1,** P13 (2009).

170. Hu, L., Hecht, D. S. & Grüner, G. Percolation in Transparent and Conducting Carbon Nanotube Networks. *Nano Lett.* **4,** 2513–2517 (2004).

171. Wu, H. *et al.* Electrospun Metal Nanofiber Webs as High-Performance Transparent Electrode. *Nano Lett.* **10,** 4242–4248 (2010).

172. Rathmell, A. R., Bergin, S. M., Hua, Y.-L., Li, Z.-Y. & Wiley, B. J. The Growth Mechanism of Copper Nanowires and Their Properties in Flexible, Transparent Conducting Films. *Adv. Mater.* **22,** 3558–3563 (2010).

173. Panel, T. Touch Panel. 1–65 (2010).

174. Bergin, S. M. *et al.* Nanoscale The effect of nanowire length and diameter on the properties of transparent , conducting nanowire films †. (2012). doi:10.1039/c2nr30126a

175. Lee, J. Y., Connor, S. T., Cui, Y. & Peumans, P. Solution-processed metal nanowire mesh transparent electrodes. *Nano Lett.* **8,** 689–692 (2008).

176. Ghosh, D. S., Martinez, L., Giurgola, S., Vergani, P. & Pruneri, V. Widely transparent electrodes based on ultrathin metals. *Opt. Lett.* **34,** 325–327 (2009).

177. Bao, W. *et al.* Approaching the limits of transparency and conductivity in graphitic materials through lithium intercalation. *Nat. Commun.* **5,** 4224 (2014).

178. Lin, M.-C. *et al.* An ultrafast rechargeable aluminium-ion battery. *Nature* (2015). doi:10.1038/nature14340